Tuning site-specific dynamics to drive allosteric activation in a pneumococcal zinc uptake regulator

Daiana A. Capdevila,[†] Fidel Huerta,[†,‡] Katherine A. Edmonds,[†] My T. Le,[†] Hongwei Wu,[†] and David P. Giedroc*[,†,§]

[†]*Department of Chemistry*, Indiana University, 800 E. Kirkwood Drive, Bloomington, IN 47405-7102, United States

[‡]*Graduate Program in Biochemistry*, Indiana University, 212 S. Hawthorne Drive, Bloomington, IN 47405, United States

[§]*Department of Molecular and Cellular Biochemistry*, Indiana University, 212 S. Hawthorne Drive, Bloomington, IN 47405 United States

Correspondence to David P. Giedroc: giedroc@indiana.edu

Abstract

MarR (multiple antibiotic resistance repressor) family proteins are bacterial repressors that regulate transcription in response to a wide range of chemical signals. Although specific features of MarR family function have been described, the role of atomic motions in MarRs remains unexplored thus limiting insights into the evolution of allostery in this ubiquitous family of repressors. Here, we provide the first experimental evidence that internal dynamics play a crucial functional role in MarR proteins. Streptococcus pneumoniae AdcR (adhesin-competence repressor) regulates Zn^{II} homeostasis and Zn^{II} functions as an allosteric activator of DNA binding. Zn^{II} coordination triggers a transition from independent domains to a more compact structure. We identify residues that impact allosteric activation on the basis of Zn^{II}-induced perturbations of atomic motions over a wide range of timescales. These findings reconcile the distinct allosteric mechanisms proposed for other MarRs and highlight the importance of conformational dynamics in biological regulation.

Introduction

Successful bacterial pathogens respond to diverse environmental insults or changes in intracellular metabolism by modulating gene expression (Alekshun & Levy, 2007). Such changes in gene expression are often mediated by "one-component" transcriptional regulators, which directly sense chemical signals and convert such signals into changes in transcription. Members of the multiple antibiotic resistance regulator (MarR) family are critical for the survival of pathogenic bacteria in hostile environments, particularly for highly antibiotic-resistant pathogens (Ellison & Miller, 2006, Yoon *et al.*, 2009, Weatherspoon-Griffin & Wing, 2016, Tamber & Cheung, 2009, Aranda *et al.*, 2009, Grove, 2017). Chemical signals sensed by MarRs include small molecule metabolites (Deochand & Grove, 2017), reactive oxygen species (ROS) (Liu *et al.*, 2017, Sun *et al.*, 2012) and possibly reactive sulfur species (RSS) (Peng *et al.*, 2017). It has been proposed that evolution of new MarR proteins enables micro-organisms to colonize new niches (Deochand & Grove, 2017), since species characterized by large genomes and a complex lifestyle encode many, and obligate parasitic species with reduced genome sizes encode few (Perez-Rueda *et al.*, 2004). Therefore, elucidating how new inducer specificities and responses have evolved in this ubiquitous family of proteins on what is essentially an unchanging molecule scaffold is of great interest, as is the molecular mechanism by which inducer binding or cysteine thiol modification allosterically regulates DNA operator binding in promoter regions of regulated genes.

Obtaining an understanding of how allostery has evolved in one-component regulatory systems (Ulrich *et al.*, 2005, Marijuan *et al.*, 2010), including MarR family repressors, requires a comprehensive analysis of the structural and dynamical changes that occur upon inducer and DNA binding (Capdevila *et al.*, 2017a, Tzeng & Kalodimos, 2013, West *et al.*, 2012, Tzeng & Kalodimos, 2009). For MarRs, several distinct allosteric mechanisms have been proposed, from

a "domino-like" response (Bordelon *et al.*, 2006, Gupta & Grove, 2014, Perera & Grove, 2010) to ligand binding-mediated effects on asymmetry within the dimer (Anandapadamanaban *et al.*, 2016), to oxidative crosslinking of *E. coli* MarR dimers into DNA binding-incompetent tetramers (Hao *et al.*, 2014). While there are more than 130 crystal structures of MarR family repressors in different allosteric states (Fig. S1), an understanding of the role of atomic motions and the conformational ensemble in MarRs is nearly totally lacking and what is known is based exclusively on simulations (Anandapadamanaban *et al.*, 2016, Sun *et al.*, 2012). Here, we provide the first experimental evidence in solution that internal dynamics play a crucial functional role in a MarR protein, thus define characteristics that may have impacted the evolution of new biological outputs in this functionally diverse family of regulators.

In the conventional regulatory paradigm, the binding of a small molecule ligand, or the oxidation of conserved ROS-sensing cysteines induces a structural change in the homodimer that typically negatively impacts DNA binding affinity. This results in a weakening or dissociation of the protein-DNA complex and transcriptional derepression. Several reports provide evidence for a rigid body reorientation of the two α4 (or αR)-reading heads within the dimer (Fig. 1A-B, Fig. S1) (Alekshun *et al.*, 2001, Fuangthong & Helmann, 2002, Wilke *et al.*, 2008, Chang *et al.*, 2010, Liu *et al.*, 2017, Deochand & Grove, 2017, Dolan *et al.*, 2011, Deochand *et al.*, 2016). The generality of this simple paradigm is inconsistent with the findings that some MarR proteins share very similar static structures in the active (DNA binding-competent) and inactive (DNA binding-incompetent) states (Anandapadamanaban *et al.*, 2016, Kim *et al.*, 2016, Liguori *et al.*, 2016); furthermore, several active states have been shown to require a significant rearrangement to bind DNA (Alekshun *et al.*, 2001, Liu *et al.*, 2017, Zhu *et al.*, 2017b, Hao *et al.*, 2013, Gao *et al.*, 2017, Chin *et al.*, 2006, Saridakis *et al.*, 2008). In fact, a comprehensive analysis of all available MarR family structures strongly suggests that the degree of structural reorganization

82 required to bind DNA, characterized by a narrow distribution of α4-α4' orientations, is
83 comparable whether transitioning from the inactive *or* active states of the repressor (Fig. 1C,
84 Table S1). These observations strongly implicate a conformational ensemble model of allostery
85 (Motlagh *et al.*, 2014) (Fig. 1B-D), where inducer sensing impacts DNA binding by restricting
86 the conformational spread of the active repressor, as was proposed in a recent molecular
87 dynamics study (Anandapadamanaban *et al.*, 2016).
88 MarR proteins are obligate homodimers that share a winged-helical DNA-binding
89 domain connected to a DNA-distal all-helical dimerization domain where organic molecules
90 bind in a cleft between the two domains (Fig. S1B). Individual MarR members have been shown
91 to bind a diverse range of ligands at different sites on the dimer (Otani *et al.*, 2016, Takano *et al.*,
92 2016); likewise, oxidation-sensing cysteine residues are also widely distributed in the dimer
93 (Fuangthong & Helmann, 2002, Liu *et al.*, 2017, Hao *et al.*, 2014, Dolan *et al.*, 2011, Chen *et al.*,
94 2006). This functional diversity is accompanied by relatively low overall sequence similarity,
95 which suggests that a conserved molecular pathway that connects sensing sites and the DNA
96 binding heads is highly improbable. Complicating our current mechanistic understanding of this
97 family is that for many members, including *E. coli* MarR, the physiological inducer (if any) is
98 unknown, rendering functional conclusions on allostery from crystallographic experiments alone
99 less certain (Hao *et al.*, 2014, Zhu *et al.*, 2017b).
100 In contrast to the extraordinary diversity of thiol-based switching MarRs, MarR family
101 metallosensors are confined to a single known regulator of Zn^{II} uptake, exemplified by AdcR
102 (adhesin competence regulator) from *S. pneumoniae* and closely related *Streptococcus ssp*. (Loo
103 *et al.*, 2003, Reyes-Caballero *et al.*, 2010) and ZitR from *Lactococcus spp* (Llull *et al.*, 2011,
104 Zhu *et al.*, 2017c). AdcR and ZitR both possess two closely spaced pseudotetrahedral Zn^{II}
105 binding sites termed site 1 and site 2 (Fig. 1A) that bind Zn^{II} with different affinities (Reyes-

Caballero *et al.*, 2010, Guerra *et al.*, 2011, Sanson *et al.*, 2015, Zhu *et al.*, 2017c). Zn^{II} is an allosteric *activator* of DNA operator binding which is primarily dependent on the structural integrity of site 1 (Reyes-Caballero *et al.*, 2010, Zhu *et al.*, 2017c). ZitR has been recently extensively structurally characterized, with crystallographic models now available for the apo- and Zn^{II}_1- (bound to site 1) and Zn^{II}_2- and Zn^{II}_2-DNA operator complexes, thus providing significant new insights into ZitR and AdcR function (Zhu *et al.*, 2017c). These structures reveal that Zn^{II}_2-ZitR and Zn^{II}_2-AdcR form triangularly-shaped homodimers and are essentially identical, as anticipated from their high sequence identity (49%). Apo-ZitR adopts a conformation that is incompatible with DNA binding, and filling of both Zn^{II} sites is required to adopt a conformation that is similar to that of the DNA-complex. Thermodynamically, filling of the low affinity site 2 enhances allosteric activation of DNA-binding by ≈10-fold, and this occurs concomitant with a change in the H42 donor atom to the site 1 Zn^{II} ion from Nε2 in the apo- and Zn^{II}_1-states to Nδ1 in the Zn^{II}_2-ZitR (as in Zn^{II}_2 AdcR; (Guerra *et al.*, 2011)) and Zn^{II}_2 ZitR-DNA operator complexes (Zhu *et al.*, 2017c). Allosteric *activation* by Zn^{II} is in strong contrast to all other members of the MarR superfamily, consistent with its biological function as uptake repressor at high intracellular Zn^{II}.

Here we employ a combination of NMR-based techniques and small angle x-ray scattering (SAXS) to show that apo- (metal-free) AdcR in solution is characterized by multiple independent domains connected by flexible linkers, resulting in a distinct quaternary structure from the Zn-bound state previously structurally characterized (Guerra *et al.*, 2011). Our backbone relaxation dispersion-based NMR experiments show that apo-AdcR samples distinct conformational states in the μs-ms timescale, while Zn^{II} narrows this distribution by conformational selection, increasing the population of a state that has higher affinity for DNA. This finding is fully consistent with the crystallographic structures of Zn^{II}_2 ZitR and the Zn^{II}_2

ZitR:DNA complex (Zhu *et al.*, 2017c). The site-specific backbone and methyl sidechain dynamics in the ps-ns timescale show that Zn^{II} not only induces a general restriction of these protein dynamics, but also enhances fast timescale, low-amplitude motions in the DNA binding domains. Together, these data reveal that Zn^{II} coordination promotes a conformational change that reduces the entropic cost of DNA binding and enhances internal dynamics uniquely within the DNA binding domain, thus poising the repressor to interact productively with various DNA operator target sequences (Reyes-Caballero *et al.*, 2010). We demonstrate the predictive value of this allosteric model by functionally characterizing "cavity" mutants of AdcR (Capdevila *et al.*, 2017a). Overall, our findings suggest that protein dynamics on a wide range of timescales strongly impact AdcR function. This ensemble model of allostery successfully reconciles the distinct mechanisms proposed for other MarR family repressors and suggests a mechanism of how evolution tunes dynamics to render distinct biological outputs (allosteric activation vs. allosteric inhibition) on a rigorously conserved molecular scaffold.

Results and Discussion

Solution structural differences between apo and Zn^{II} bound forms of AdcR

Our crystal structure suggests that once AdcR is bound to both Zn^{II}, the αR- (α4) reading heads adopt a favorable orientation for DNA binding (Guerra *et al.*, 2011), a finding fully compatible with structural studies of *L. lactis* ZitR (Zhu *et al.*, 2017c) (Fig. 1A). These structural studies suggest a "pre-locked" model, where Zn^{II} binding to both sites 1 and 2, concomitant with a H42 ligand atom switch, locks the AdcR homodimer into a DNA binding-competent conformation. This model makes the prediction that the unligated AdcR can explore conformations structurally incompatible with DNA binding, as shown previously for Zn^{II}_1 ZitR (Zhu *et al.*, 2017c), thus requiring a significant degree of reorganization to bind with high

affinity to the DNA (Fig. 1B). Despite significant efforts, it has not yet been possible to obtain the crystal structure of apo-AdcR, suggesting that the apo-repressor may be highly flexible in solution (Guerra *et al.*, 2011, Sanson *et al.*, 2015). Thus, we employed SAXS as a means to explore the apo-AdcR structure and elucidate the structural changes induced by Zn^{II} binding and conformational switching within the AdcR homodimer.

We first examined the behavior of apo- and Zn^{II}-bound states. Both states show Guinier plots indicative of monodispersity and similar radii of gyration (R_g). These data reveal that each state is readily distinguished from the other in the raw scattering profiles (to q=0.5 $Å^{-1}$) as well as in the PDDF plots (*p(r) versus r*), with the experimental scattering curve of the Zn^{II} bound state being consistent with one calculated from the Zn^{II}_2 AdcR crystal structure (Fig. 2A). Moreover, a qualitative analysis of the PDDF plots suggests that apo-AdcR is less compact than the Zn^{II}-bound state (Fig. S2). The molecular scattering envelopes calculated as bead models with the *ab initio* program DAMMIF for apo-AdcR suggest that the differences between the apo and Zn^{II} AdcR SAXS profiles can be explained on the basis of a reorientation of the winged helix-turn-helix motif with respect to the dimerization domain, particularly in a distortion in the α5 helix (Fig. 2B). In an effort to obtain higher resolution models, we reconstructed atomic models from perturbations in the Zn-bound crystal structure that better fit the complete SAXS profiles (q<1.0). The models obtained confirm that the Zn-bound structure in solution resembles the crystallographic models of apo-ZitR and Zn^{II} AdcR (Guerra *et al.*, 2011, Zhu *et al.*, 2017c); however, we note that the SAXS profile of the apo-AdcR differs significantly from the ZitR crystal structure (Fig. S2E) which is likely related to the high flexibility of this state in solution. Moreover, the resolution of SAXS based models cannot be used to obtain residue-specific information about structural perturbations introduced by Zn^{II} binding (Fig. S2). Thus, we turned

177 to NMR-based techniques to provide both high resolution and site-specific information on this
178 highly dynamic system.

179 TROSY NMR on 100% deuterated AdcR and optimized buffer conditions for both states
180 (pH 5.5, 50 mM NaCl, 35 ºC) enabled us to obtain complete backbone assignments for Zn^{II}-
181 AdcR and nearly complete for apo-AdcR (missing residues 21, 38-40 due to exchange
182 broadening, Fig. 3). The chemical shift perturbation maps (Fig. 3A-B) reveal that the largest
183 perturbations are found in the structural vicinity of the metal site region, *i.e.*, the α1-α2 loop
184 (residues 21-35), the remainder of the α2 helix (residues 41-47), and the central region of the α5
185 helix, which provides donor groups to both site 1 (H108, H112) and site 2 (E107) Zn^{II}. These
186 changes derive from changes in secondary structure, such as the extension of the α1 helix and
187 partial unfolding of the α2 helix (Fig. S3), as well as from proximity to the Zn^{II}.

188 The changes in carbon chemical shifts in the central region of the α5 helix and the
189 presence of strong NOEs to water for these residues are consistent with a kink in this helix in the
190 apo-state (Fig. S3A-B), as is commonly found in other structurally characterized MarR
191 repressors in DNA-binding inactive conformations (Zhu *et al.*, 2017b, Duval *et al.*, 2013).
192 However, the kink is expected to be local and transient, since a TALOS+ analysis of chemical
193 shifts predicts that the α5 helix remains the most probable secondary structure for all tripeptides
194 containing these residues in the apo-state (Shen *et al.*, 2009) (Fig. S3C). The backbone changes
195 in chemical shifts are accompanied by changes in the hydrophobic cores in the proximity of Zn^{II}
196 binding as reported by the stereospecific sidechain methyl group chemical shift perturbation
197 maps (Fig. 3B). Comparatively smaller perturbations extend to the α1 helix and the C-terminal
198 region of the α6 helix, DNA-binding α4 helix (S74) and into the β-wing itself, consistent with a

significant change in quaternary within the AdcR homodimer upon binding of both allosteric metal ions (Fig. 3A-B).

Overall, our NMR and SAXS data show that the main structural differences are localized in the region immediately surrounding the Zn^{II} coordination sites, giving rise to a change in the quaternary structure, while conserving the size and the overall secondary structure of the molecule. In particular, our data point to a kink in the α5 helix and a structural perturbation in the α1-α2 loop, which could be inducing a reorientation of the winged helix-turn-helix motifs relative to the dimerization domain.

In an effort to understand the functional consequences of the structural perturbations in the α1-α2 loop, we compared the length of the loop that connects the dimerization domain with the winged helical motif among AdcR and other members of the MarR family of known structure. This structural comparison and an extensive multiple sequence alignment reveals that only AdcR-like repressors harbor an α1-α2 loop larger than 10 residues (Fig. 3C). This loop extension does not seem to originate from an insertion, but from a change in secondary structure of the C-terminal region of the α1 helix (Fig. 3C). Moreover, in the Zn^{II} state that loop appears restricted by a hydrogen-bond network between the Zn^{II} binding site and the DNA binding domain (Chakravorty *et al.*, 2013). The Zn^{II}-ZitR crystal structure similarly has an α1-α2 loop that is restricted by metal coordination chemistry and other intermolecular contacts with the dimerization and DNA binding domains, despite lacking an identifiable hydrogen-bond network (Zhu *et al.*, 2017c). Overall, our analysis suggests that the flexibility of this loop prevents DNA-binding, while the interactions formed in response to Zn^{II} coordination may be important in allosteric activation of DNA binding. Such a dynamical model contrasts sharply with a rigid body motion mechanism as previously suggested for other MarRs (Alekshun *et al.*, 2001, Chang

et al., 2010, Dolan *et al.*, 2011, Saridakis *et al.*, 2008, Birukou *et al.*, 2014, Radhakrishnan *et al.*, 2014), thus motivating efforts to understand how conformational dynamics impacts biological regulation by Zn^{II} in AdcR.

Zn^{II}-induced changes in AdcR conformational plasticity along the backbone

We therefore turned to an investigation of protein dynamics in AdcR. ^{15}N R_1, R_2, and steady-state heteronuclear $^{15}N\{^1H\}$ NOEs provide information on internal mobility along the backbone, as well as on the overall protein tumbling rate (Fig. 4A-D; Fig. S4). The R_1 and R_2 data reveal that Zn^{II}_2 AdcR tumbles predominantly as a single globular unit in solution (Fig. 4B; Fig. S4) with a molecular correlation time (τ_c) of 18.7 ± 0.1 ns, very similar to the τ_c value predicted for the dimer at 35 ºC (18.9 ns in D_2O). The β-wing region tumbles independently from the rest of the molecule (Fig. 4B). These data also reveal that the α1-α2 linker region that donates the E24 ligand to Zn^{II} binding site 1 is ordered to an extent similar to the rest of the molecule. In striking contrast, in apo-AdcR, the dimerization and DNA-binding domains have significantly smaller τ_c values (10.9 ± 0.5 ns, Fig. 4A), close to that expected if these domains tumble independently of one another in solution; in addition, the α1-α2 loop is highly dynamic in the apo-state (see also Fig. S4). These findings are consistent with the SAXS data, which show that apo-AdcR is less compact than the Zn^{II}_2 state. As in the Zn^{II}_2 state, the β–wing tumbles independently of the rest of the molecule, revealing that a change in the flexibility or orientation of the β–hairpin is likely not part of the allosteric mechanism, contrary to what has been proposed for other MarRs on the basis of crystal structures alone (Liu *et al.*, 2017, Deochand & Grove, 2017, Kim *et al.*, 2016). Overall, the ^{15}N relaxation data for backbone amides show that Zn^{II} binding leads to a reduction of mobility of the α1-α2 loop, which in turn,

245 decreases the dynamical independence the DNA-binding and dimerization domains, thereby
246 stabilizing a conformation that tumbles in solution as a single globular unit.

247 To further probe the reduction of flexibility upon Zn^{II} binding, we investigated sub-
248 nanosecond backbone mobility as reported by the steady-state heteronuclear $^{15}N\{^{1}H\}$ NOEs
249 (Fig. 4C-D). These hNOE data confirm that the internal mobility of the apo-state on this
250 timescale mainly localizes to the α1-α2 loop and the central region of the α5 helix, around E107
251 (Zn^{II} site 2 ligand) and H108 and H112 (Zn^{II} site 1 ligands). The short-timescale flexibility in
252 this region is significantly restricted upon Zn^{II} binding, but somewhat paradoxically leads to an
253 *increase* in sub-nanosecond backbone motion in the DNA-binding domain, particularly in the α3
254 helix and the N-terminal region of the α4 helix, which harbors the key DNA-binding
255 determinants (Fig. S1A) (Zhu *et al.*, 2017c). The quenching of sub-nanosecond mobility in the
256 α1-α2 loop by Zn^{II} is accompanied by a corresponding increase in mobility on the μs-ms (slow)
257 timescale in this region (Fig. 4F). In addition, the slow timescale backbone dynamics show a
258 restriction of a conformational sampling in a band across the middle of the dimerization domain,
259 including the upper region of the α5 helix, the N-terminus of α1, and the C-terminus of α6 (Fig.
260 4E-F). These slow motions in the apo-state likely report on a global breathing mode of the
261 homodimer reflective of the conformational ensemble, which is substantially restricted upon Zn^{II}
262 binding.

263 These large differences in structure and dynamics between the apo and Zn^{II}_2 AdcRs
264 suggest an allosteric mechanism that relies on a redistribution of internal mobility in both fast-
265 and slow timescale regimes, rather than one described by a rigid body motion. This mobility
266 redistribution restricts the flexibility of the ligand binding site from the sub-nanosecond
267 timescale in the apo-form to the millisecond timescale in the Zn^{II}_2 state (Fig. 4C,F). This

restriction links the motion of the two functional domains (Fig. 4A-B) and locks AdcR in a triangular shape compatible with DNA binding. On the other hand, Zn^{II} enhances the internal flexibility in the DNA binding domain (Fig. 4C-D), which other studies show plays a role in sequence recognition and high affinity binding, particularly on the side chains (Capdevila *et al.*, 2017a, Kalodimos *et al.*, 2004, Anderson *et al.*, 2013).

Zn^{II}-induced perturbations of side chain conformational disorder in AdcR

Unlike the backbone, perturbations in side chain flexibility in the sub-nanosecond timescale are capable of reporting on the underlying thermodynamics of Zn^{II} binding and the role of conformational entropy (ΔS_{conf}) in the allosteric mechanism. These perturbations potentially pinpoint residues with functional roles, *i.e.*, allosteric hotspots (Capdevila *et al.*, 2017a), with the change in the methyl group order parameter (ΔS^2_{axis}) upon ligand binding employed as a dynamical proxy (Capdevila *et al.*, 2017a, Caro *et al.*, 2017). Thus, if the motional redistribution observed in the backbone upon Zn^{II} binding is accompanied by changes in the dynamics on the side chains, particularly those in the DNA binding regions, these fast internal dynamics could affect the entropy of the metal binding and play a major role in the allosteric mechanism. To test these ideas, we first measured the axial order parameter, S^2_{axis}, for all 82 methyl groups, comparing the apo- and Zn-bound states of AdcR (Fig. 5A, Fig. S5). These dynamics changes are overall consistent with the stiffening observed along protein backbone, *e.g.,* in the α1-α2 loop; L26, in particular, is strongly impacted, changing motional regimes, $|\Delta S^2_{axis}|>0.2$) (Frederick *et al.*, 2007). This stiffening prevails all over the molecule, leading to a small net decrease in conformational entropy upon Zn^{II} coordination ($-T\Delta S_{conf}= 3.4 \pm 0.4$ kcal mol^{-1}) (Fig. 5A). However, as has been previously shown for other transcriptional regulators (Capdevila *et al.*, 2017a, Tzeng & Kalodimos, 2012), the binding of the allosteric ligand Zn^{II} actually leads to a

redistribution of sidechain mobility throughout the entire molecular scaffold. Interestingly, most of the methyl groups that change motional regimes are located in the DNA binding domain (Fig. S7). In particular, the side chain flexibility of many residues in the α3 helix *increases*, including L47, L57, L61, while a small hydrophobic core in the C-terminus of the α4 helix stiffens significantly, *e.g.,* L81, V34. These changes are accompanied by perturbations in the dynamics at the dimer interface, *i.e.,* L4, I16, V14, in both motional regimes as reported by ΔS^2_{axis} and ΔR_{ex} (in the μs-ms timescale), the latter derived from relaxation dispersion experiments (Table S2; Fig. S5C).

On-pathway and off-pathway allosterically impaired mutants of AdcR

Our previous work (Capdevila *et al.*, 2017a) makes the prediction that "dynamically active" sidechains (methyl groups with $|\Delta S^2_{axis}| \geq 0.2$ upon Zn^{II} binding) (see Fig. 5) are crucial for allosteric activation of DNA binding by Zn^{II}. To test this prediction, we prepared and characterized several mutant AdcRs in an effort to disrupt allosteric activation of DNA binding, while maintaining the structure of the dimer and high affinity Zn^{II} binding. Since it was not clear *a priori* how mutations that perturb mobility distributions in one timescale or the other (sub-ns or μs-ms) would impact function, we focused on two kinds of substitution mutants: cavity mutants of dynamically "active" methyl-bearing side chains positioned in either the DNA binding or the dimerization subdomains (Fig. 6A, B) (Capdevila *et al.*, 2017a), and substitutions in the hydrogen-bonding pathway in the Zn-state that may contribute to the rigidity of the α1-α2 loop in Zn^{II}_2-AdcR (Fig. 6A) (Chakravorty *et al.*, 2013). We measured DNA binding affinities of the apo and zinc-saturated Zn^{II}_2-states, and calculated the allosteric coupling free energy, ΔG_c, from $\Delta G_c = -RT\ln(K_{Zn,DNA}/K_{apo,\ DNA})$ (Giedroc & Arunkumar, 2007) (Fig. 6C and Table S2). All

315 mutants are homodimers by size-exclusion chromatography (Fig. S9) and all bind the first
316 equivalent of Zn^{II} tightly as wild-type AdcR (Fig. S10, Table S3).

317 *DNA-binding domain mutants.* The redistribution fast time scale side-chain dynamics in
318 the DNA binding domain is delocalized throughout the different secondary structure motifs.
319 Thus, we prepared several cavity mutants of methyl-bearing residues in the α3 (L57, L61), α4
320 (L81) and α5 (I104) helices, as well as two residues in the α1-α2 loop in close proximity to the
321 N-terminus of α2, V34 and L36. I104 is the most distal from the bound DNA in the Zn^{II}_2 ZitR-
322 DNA complex (Zhu *et al.*, 2017c), and is not dynamically active in AdcR ($|\Delta S^2_{axis}|<0.1$;
323 $\Delta R_{ex}<1.0$); thus, the I104A mutant is predicted to function as a control substitution. V34 and L36
324 are dynamically active on both timescales, which is not surprising since the α1-α2 loop folds
325 upon Zn^{II} binding to AdcR (*vide supra*) (Zhu *et al.*, 2017c). In contrast, L57, L61 and L81 are
326 characterized by significant perturbations in ΔS^2_{axis} only ($|\Delta S^2_{axis}|\geq0.2$), with L81 stiffening and
327 L57 and L61 methyls in the α3 helix becoming significantly more dynamic upon Zn^{II} binding
328 (Fig. 5A, Table S2).

329 As expected, I104A AdcR is characterized by DNA binding affinities in the apo- and Zn-
330 states just ≈2-fold lower than wild-type AdcR, returning a ΔG_c that is not statistically different
331 from wild-type AdcR (Fig. 6C). Functional characterization of all other cavity mutants in the
332 DNA binding domain results in a ≈5-10-fold decrease or greater (L57V AdcR; Table S2) in the
333 DNA binding affinity of the apo-state (Fig. 6C), with Zn^{II} binding inducing markedly variable
334 degrees of allosteric activation (Fig. 6C). L36A, closest to the α2 N-terminus, is most like wild-
335 type AdcR, while V34A AdcR is severely crippled in allostery, with $K_{Zn,DNA}$ some 200-fold
336 lower than wild-type AdcR, and ΔG_c ≈2-fold lower, from –4.0 to –2.2 kcal mol^{-1}. L81V and
337 L61A AdcRs are comparably perturbed, and L57M AdcR even more so (ΔG_c≈–2.0 kcal mol^{-1}).

We emphasize that these methyl-bearing side chains targeted for substitution are ≥95% buried and none are expected to be in direct contact with the DNA (Fig. 6B, Table SI). These data provide strong support for the idea that those methyl-bearing side chains in the DNA-binding domain that exhibit large changes in conformational entropy (as measured by ΔS^2_{axis}) make significant contributions to both DNA binding and allosteric activation by Zn^{II}. This result highlights the contribution that dynamical redistribution within the DNA-binding domain makes for AdcR function, as has been observed in other transcriptional regulators (Tzeng & Kalodimos, 2012; Capdevila *et al*., 2017a).

Hydrogen-bonding mutants. A hydrogen-bonding pathway in AdcR (Chakravorty *et al.*, 2013) has previously been proposed to transmit the Zn^{II}_2 binding signal to the DNA binding domain. In this pathway, the Oε1 atom from the Zn^{II} ligand E24 accepts a hydrogen bond from the carboxamide side chain of N38. N38 is the +1 residue of the α2 helix, which is then connected to the α4 helix via a hydrogen bond between the Q40 and S74 side chains; further, Q40 accepts a hydrogen bond from the γ-OH of T37 as part of a non-canonical helix N-capping interaction (Guerra *et al.*, 2011) (Fig. 6A). We expect that regardless of the impact that these interactions have on the overall energetics of Zn^{II} binding, they are important in the restriction of fast-time scale dynamics in the α1-α2 loop. We therefore targeted residues E24 (Zn-ligand and H-bound acceptor), N38 and Q40, by characterizing two single mutants, E24D and N38A, and the double mutant, N38A/Q40A AdcR. Although all three mutants undergo allosteric switching as revealed by $^{1}H–^{15}N$ TROSY spectra (Fig. S11), as with all other DNA-binding domain mutants, all three exhibit ≈5-10-fold decreases in apo-state DNA-binding affinity (Fig. 6C; Table S2). While the single mutant N38A binds Zn^{II} to give ΔG_c of ≈–3.5 kcal mol^{-1}, quite similar to that of wild-type AdcR, in marked contrast, N38A/Q40A AdcR is functionally perturbed, characterized by a ΔG_c of ≈–1.9 kcal mol^{-1} and is E24D AdcR that target a Zn^{II} binding residue

(Fig. 6C). These perturbations provide additional evidence that this hydrogen-bonding pathway may contribute to the motional restriction of the α1-α2 loop, jointly with a redistribution of internal dynamics in the DNA binding domain. This effect can be perturbed directly by mutation of "dynamically active" sidechains (L81V, L61V, L57M) or by significantly impacting the interactions that restrict the loop (N38A/Q40A).

Dimerization domain mutants. To test the functional role of the dimerization domain in dynamical changes, we targeted three methyl-bearing residues in this domain, including L4 and I16 on opposite ends of the α1 helix and V142, near the C-terminus of the α6 helix (Fig. 6B). L16 is closest to the intervening minor groove of the DNA operator, while V142 and L4 are increasingly distant from the DNA. These residues are primarily active in slow timescale dynamics, with Zn^{II}-binding quenching side chain mobility on the μs-ms timescale, *i.e.,* global motions, but relatively smaller changes in ΔS^2_{axis} (Fig. 5B; Table S2). Cavity mutants of these residues (I16A, L4A and V142A) bind DNA in the apo-state with wild-type like affinities, but each is allosterically strongly perturbed, with only ≈10-20-fold allosteric activation by Zn^{II}, giving ΔG_c values of –1.4 to –1.8 kcal mol^{-1}.

These findings suggest that Zn^{II}-dependent quenching of global motions far from the DNA binding domain play a significant role in allostery in this system. Our characterization of allosterically compromised mutants that affect site-specific conformational entropy (L81V, L61V, L57M) and conformational exchange (V34A, L4A, I16A) provides evidence for two classes of functional dynamics in AdcR that comprise different regions of the molecule, operating on different timescales (from sub-nanoseconds to milliseconds). Thus, we propose that a Zn^{II}-dependent redistribution of internal dynamics quenches global, slow motions in the dimer, yet enhances local dynamical disorder in the DNA binding domain, which can ultimately be harnessed to maximize contacts at the protein-DNA interface.

Conclusions

Members of the multiple antibiotic resistance repressor (MarR) family of proteins comprise at least 12,000 members (Capdevila *et al.*, 2017b), and many have been subjected to significant structural inquiry since the original discovery of the *E. coli mar* operon and characterization of *E. coli* MarR some 25 years ago (Cohen *et al.*, 1993, Seoane & Levy, 1995). The crystallographic structure of this prototypical *E. coli* MarR appeared a number of years later (Alekshun *et al.*, 2001) and has inspired considerable efforts to understand the inducer specificity and mechanisms of transcriptional regulation in *E. coli* MarR (Hao *et al.*, 2014) and other MarR family repressors (Grove, 2013), which collectively respond to an wide range of stimuli, including small molecules, metal ions, antibiotic and oxidative stress (Deochand & Grove, 2017). We have examined the wealth of the crystallographic data available from 137 MarR family repressor structures solved in a variety of functional states, including DNA-binding competent, DNA-binding incompetent and DNA-bound states (Fig. 1). This analysis of the crystal structures suggests that conformational selection induced by ligand binding or thiol oxidation must be operative in a significant number of these repressor systems. Here, we present the first site-specific dynamics analysis of any MarR family repressor in solution, and establish that conformational dynamics on a range of timescales is a central feature of Zn^{II}-dependent allosteric activation of DNA operator binding by the zinc uptake regulator, *S. pneumoniae* AdcR (Reyes-Caballero *et al.*, 2010) and closely related repressors (Zhu *et al.*, 2017c).

We explored dynamics in the sub-nanosecond and µs-ms timescales with residue-specific resolution, both along the backbone, as measured by N-H bond vectors, and in the methyl groups of the methyl-bearing side chains of Ala, Met, Val, Leu and Ile. These measurements, coupled with small angle x-ray scattering measurements of both conformational states, lead to a consistent picture of allosteric activation by Zn^{II} in AdcR. The apo-state conformational

ensemble is far broader than the Zn^{II}_2 state, and features dynamical uncoupling of the core DNA-binding and dimerization domains, facilitated by rapid, low amplitude motions in the α1-α2 loop and the α5 helix in the immediate vicinity of the Zn^{II} coordinating residues. This motion is superimposed on a much slower, larger amplitude mobility across the dimerization domain, far from the DNA interface, affecting both backbone amide and side chain methyl groups (Fig. 4-5). Zn^{II} binding substantially quenches both the low amplitude internal motions and global, larger amplitude movements, while driving a striking redistribution of these dynamics into the DNA-binding domain.

As we observed previously for another Zn^{II} metalloregulatory protein, Zn^{II} binding induces a net global conformational stiffening, superimposed on pockets of increased dynamical disorder, particularly in the α3-α4 region of the DNA binding domain (Fig. 5A). It is interesting to note that the structures of Zn^{II}_2-bound AdcR and DNA-bound Zn^{II}_2 ZitR differ most strongly in the α3-α4 region (Fig. 6B), suggesting that internal dynamics in this region may be functionally important in enhancing DNA binding affinity. To test the functional importance of fast-time scale motions in the DNA binding domain, we exploited the side chain dynamics results (Fig. 5) (Capdevila *et al.*, 2017a) to design cavity substitutions of dynamically active residues (Fig. 6). We generally find that cavity substitutions in the DNA binding domain are strongly deleterious for residues that are dynamically active in the fast timescale ($|\Delta S^2_{axis}|>0.2$), *i.e.* L81, L61, L57. These findings confirm a functional role of these changes in dynamics (Capdevila *et al.*, 2017a) and suggest that Zn^{II}_2-bound AdcR has an optimal distribution of internal dynamics that if perturbed, leads to weakened DNA binding.

Crystallographic studies suggest that DNA binding in MarR repressors is optimized by precisely tuning interactions with the DNA operator sequence, resulting in a favorable ΔH of

433 binding (Hong *et al.*, 2005, Dolan *et al.*, 2011, Quade *et al.*, 2012, Birukou *et al.*, 2014, Zhu *et*
434 *al.*, 2017a, Gao *et al.*, 2017, Otani *et al.*, 2016) with the functional consequences of ligand
435 binding known to vary widely among individual MarRs (Deochand & Grove, 2017). We
436 propose here, based on this and previous work, that tighter DNA binding can be achieved by
437 optimization of side-chain dynamics that give rise to a more favorable conformational entropy
438 term (ΔS_{conf}) and the functional consequences of ligand binding can be predicted based on the
439 protein internal motions. We show here that single point mutations in AdcR, sufficient to impact
440 internal motions, result in destabilization of the ternary complex. We showed previously that
441 ligand binding can inhibit formation of the DNA complex by restricting the coupled fast motions
442 and concerted slower motions that contribute to a favorable conformational entropy of DNA
443 binding (Capdevila *et al.*, 2017a). This can potentially be the case also for introduction of
444 dynamic elements, *i.e.*, loops or disordered regions (Pabis *et al.*, 2018, Campbell *et al.*, 2016).
445 Thus, in the context of evolution of the MarR repressors, we propose that two allosteric modes,
446 activation and inhibition, may have evolved by tuning the conformational entropy contribution to
447 DNA binding (Fig. 7).

448 Allosteric inhibition could have arisen by evolution of a ligand binding pocket where
449 inducer recognition disrupts internal dynamics and increases the conformational entropic cost of
450 binding to DNA, as we have previously shown for an ArsR family protein (Capdevila *et al.*,
451 2017a). Although this hypothesis has not been tested experimentally on any MarR, molecular
452 dynamics simulations show that DNA binding-impaired mutants of MexR differ from the wild-
453 type repressor in the nature of the dynamical connection between the dimerization and DNA
454 binding domains (Anandapadamanaban *et al.*, 2016). This dynamical connectivity is in fact,
455 exploited by the binding the ArmR peptide, leading to DNA dissociation (Anandapadamanaban
456 *et al.*, 2016, Wilke *et al.*, 2008). We propose that conformational entropy can contribute to other

457 mechanisms of allosteric inhibition to yield a repressor that binds tightly to the operator sequence
458 and yet has the ability to readily evolve new inducer specificities.

459 On the other hand, allosteric activation could have evolved by perturbing internal
460 dynamics on the apo-protein and increasing the conformational entropic cost of DNA binding.
461 This perturbation could arise by the introduction of loops or disordered regions in the apo-protein
462 that could be compensated by a ligand binding event that restores the internal dynamics to yield a
463 more favorable entropy contribution to DNA binding (Fig. 7). Similarly, it has been shown that
464 another well-studied, allosterically activated, bacterial regulator, catabolite activator protein
465 (CAP) (Tzeng & Kalodimos, 2013, Tzeng & Kalodimos, 2012) is able to harness conformational
466 entropy to increase DNA binding affinity upon ligand binding. In the case of MarRs, the far
467 longer α1-α2 linker in AdcRs (Fig. 3) may have been an important intermediate determinant in
468 the evolution of allostery in AdcR, given the key role this loop plays in dynamical uncoupling of
469 the dimerization and DNA-binding domains in the ligand-free state (Fig. 7).

470 This model makes the prediction that if conformational entropy can be harnessed to bind
471 DNA with high affinity, perturbations introduced by ligand binding or subtle change in protein
472 sequence that conserve the molecular scaffold can easily lead to inactivation of DNA binding
473 (Fig. 7). It is interesting to note that mutations that lead to inactivation are not necessarily part of
474 a physical pathway with the DNA binding site (Clarke *et al.*, 2016), since they only need to
475 affect dynamical properties that are likely delocalized in an extended network. Notably, single
476 point mutants in the dimerization domain of various MarR family repressors have been shown to
477 modulate allostery and DNA binding (Anandapadamanaban *et al.*, 2016, Deochand *et al.*, 2016,
478 Liguori *et al.*, 2016, Duval *et al.*, 2013, Alekshun & Levy, 1999, Andresen *et al.*, 2010). In the
479 case of AdcR, structural perturbations induced by Zn^{II} binding are essentially confined to the Zn^{II}
480 binding pocket, *i.e.,* the α1-α2 loop and the α5 helix proximal to the Zn^{II} donor ligands (Fig. 3).

In striking contrast, dynamical perturbations extend all over the molecule, and feature many residues that are far from either ligand binding site, and are dynamically active on the sub-nanosecond and/or μs-ms timescales (Figs. 4-5). Thus, the conformational entropy contribution being inherently delocalized and easily perturbed can enable rapid optimization of new inactivation mechanisms that would allow new biological functionalities to arise (Fig 7). Moreover, we suggest that changes in the site-specific dynamics, derived from differences in the amino acid sequence, could evolve allosteric activation from allosteric inhibition in the context of the same overall molecular scaffold. These findings inspire efforts to explore the evolution of allostery in this remarkable family of transcriptional repressors, by exploiting an allosterically crippled AdcR (see Fig. 6) to re-evolve functional allostery on this system.

Materials and Methods

AdcR mutant plasmid production

An overexpression plasmid for *S. pneumoniae* AdcR in a pET3a vector was obtained as previously described and was used as a template for the production of all mutant plasmids (Reyes-Caballero *et al.*, 2010). Mutant AdcR plasmids were constructed by PCR-based site-directed mutagenesis, and verified using DNA sequencing.

Protein production and purification

AdcR plasmids were transformed into either *E. coli* BL21(DE3) pLysS or Rosetta cells. *E. coli* cultures were either grown in LB media or M9 minimal media supplemented with $^{15}NH_4Cl$ as the sole nitrogen source with simple $^{1}H,^{15}N$ HSQC spectroscopy to assess the structural integrity of selected mutant proteins. Protein samples for backbone and methyl group assignments of AdcR

were isotopically labeled using published procedures as described in our previous work (Capdevila *et al.*, 2017a, Arunkumar *et al.*, 2007), with all isotopes for NMR experiments purchased from Cambridge Isotope Laboratories. Protein expression and purification were carried out essentially as previously described (Reyes-Caballero *et al.*, 2010). All proteins were confirmed to have <0.05 molar equivalents of Zn(II) as measured by atomic absorption spectroscopy and were dimeric by gel filtration chromatography. The AdcR protein concentration was measured using the estimated molar extinction coefficient at 280 nm of 2980 M^{-1} cm^{-1}.

Small angle x-ray scattering experiments

Small angle and wide angle x-ray scattering data of the apo and Zn^{II}_2 states of AdcR was collected at three different protein concentrations (5 mg/mL, 2.5 mg/mL and 1.25 mg/mL) in buffer 25 mM MES pH 5.5, 400 mM NaCl, 2 mM EDTA/10 μM $ZnCl_2$, 2 mM TCEP at sector 12ID-B at the Advanced Photo Source (APS) at Argonne National Laboratory. For each protein concentration and matching background buffer, 30 images were collected and averaged using NCI-SAXS program package. The scattering profile at each concentration was manually adjusted with the scale factor to remove the effect of concentration prior to subtraction of the scattering profile of the buffer. Scattering profiles of each protein concentration were then merged for further analysis. The GUINIER region was plotted with ln (I(q)) vs q^2 to check for monodispersity of the sample and to obtain I_0 and the radius of gyration (R_g) within the range of q_{max}*R_g <1.3. The R_g values obtained for apo-AdcR and Zn(II)-bound-AdcR are 25.5 ± 0.9Å and 23.7 ± 1.1 Å, respectively. The scattering profiles of each AdcR conformational state was then normalized with I_0. The compaction of each states of AdcR was examined using the Kratky plot for q<0.3 $Å^{-1}$. Scattering profiles for apo and Zn^{II}_2 states of AdcR were then Fourier-transformed

using GNOM of the ATSAS package to obtain the normalized pair-wise distance distribution graph (PDDF).

Ab initio modeling was performed using the program DAMMIF in a slow mode (Franke & Svergun, 2009). For each conformational state of AdcR, 10 models were obtained. These models were compared, aligned and averaged using the DAMSEL, DAMSUP, DAMAVER, DAMFILT, respectively, as described in the ATSAS package (http://www.embl-hamburg.de/bioSAXS). Normalized spatial discrepancy (NSD) between each pair of the models was computed. The model with the lowest NSD value was selected as the reference against which the other models were superimposed. Outliner models (2 models) with an NSD above mean + 2*standard deviation of NSD were removed before averaging. For refinement, the averaged envelope of the first run was used as search volume for the second round of modeling. Modeling of the envelope of apo-AdcR was restrained by enforcing P_2 rotational symmetry while that Zn^{II}_2 AdcR was restrained using compact, hallow and no-penalty constraints. Scattering profiles of crystal structures were calculated using the fast x-ray scattering (FOXS) webserver (https://modbase.compbio.ucsf.edu/foxs/) (Schneidman-Duhovny *et al.*, 2010).

Mag-fura-2 competition assays

All mag-fura-2 competition experiments were performed on an ISS PC1 spectrofluorometer in operating steady-state mode or a HP8453 UV-Vis spectrophotometer as described in our previous work (Capdevila *et al.*, 2017a, Campanello *et al.*, 2013) using the following solution conditions: 10 mM Hepes, pH 7.2, 400 mM NaCl that was chelex treated to remove contaminating metals. 10 μM protein concentration was used for all and MF2 concentration ranged from 13-16 μM. These data were fit using a competitive binding model with DynaFit (Kuzmic, 1996) to determine zinc binding affinities for wild-type and each mutant AdcR using a

four-site-nondissociable homodimer binding model, as previously described (Reyes-Caballero *et al.*, 2010) with K_{Zn}= 4.9 x 10^6 M^{-1} for mag-fura-2 fixed in these fits. K_1 and K_2 correspond to filling the two high affinity sites (site 1), and only a lower limits ($\geq 10^9$ M^{-1}) could be obtained for these sites; K_3 and K_4 were allowed to vary in the fit, and are reported in Table S3. Experiments were conducted 3 times for each AdcR variant. Errors of the binding constant parameters were estimated from global fits.

NMR spectroscopy

NMR spectra were acquired on a Varian VNMRS 600 or 800 MHz spectrometer, each equipped with a cryogenic probe, at the Indiana University METACyt Biomolecular NMR laboratory. The two-dimensional spectra were processed using NMRPipe (Delaglio *et al.*, 1995). The three-dimensional spectra were acquired using Poisson-gap non-uniform sampling and reconstructed using hmsIST (Hyberts *et al.*, 2012) and analyzed using SPARKY (Goddard & Kneller) or CARA (http://cara.nmr.ch). Typical solution conditions were ~500 μM protein (protomer), 25 mM MES pH 5.5, 50 mM NaCl, 1 mM TCEP, 0.02% (w/v) NaN_3, and 10 % D_2O. Some spectra were recorded at pH 6.0 as indicated. Our previous NMR studies of AdcR (Guerra *et al.*, 2011, Guerra & Giedroc, 2014) were carried out with samples containing ≈70% random fractional deuteration, pH 6.0, 50 mM NaCl, 35 ºC; under those conditions, the backbone amides of residues 21-26 in the α1-α2 loop and harboring zinc ligand E24 as well as the N-terminal region of the α2 helix (residues 37-40) exhibited significant conformational exchange broadening in the apo-state and could not be assigned (Guerra *et al.*, 2011). In this work, we acquired comprehensive ^1H-^{15}N TROSY-edited NMR data sets at 600 and 800 MHz for a 100% deuterated AdcR sample in both apo- and Zn_2-bound states at pH 5.5, 50 mM NaCl, 35º C. Under these conditions, only four backbone amides residues in the apo-state were broadened

beyond detection (residues 21, 38-40); all were visible and therefore assignable in the Zn^{II}_2 state. Thus, the N-terminus of the α2 helix, including N38 and Q40 are clearly exchange broadened in the apo-state. Sidechains were assigned following published procedures as described in our previous work (Capdevila *et al.*, 2017a, Arunkumar *et al.*, 2007). The Leu and Val methyl resonances were distinguished using through-bond information such as HMCMCBCA or HMCM[CG]CBCA experiments (Tugarinov & Kay, 2003) which correlate the Leu or Val methyl resonances with other side chain carbon resonances. All apo-protein samples contained 1 mM EDTA. All Zn^{II}_2 samples contained 2 monomer mol equiv of Zn(II). Chemical shifts were referenced to 2,2-dimethyl-2-silapentane-5-sulfonic acid (DSS; Sigma) (Wishart & Sykes, 1994).

S^2_{axis} of the Ile δ1, Leu δ1/δ2, Val γ1/γ2, Ala β, and Met ε methyl groups in apo and $Zn(II)_2$ states were determined using ^1H spin-based relaxation experiments at 600 MHz at 35.0 °C (Tugarinov *et al.*, 2007). S^2_{axis} values, cross-correlated relaxation rates, η, between pairs of ^1H–^1H vectors in $^{13}CH_3$ methyl groups were measured using Eq. 2

$$\eta = \frac{R^F_{2,H} - R^S_{2,H}}{2} \approx \frac{9}{10}\left(\frac{\mu_o}{4\pi}\right)^2 [P_2(cos\theta_{axis,HH})]^2 \frac{S^2_{axis}\gamma^4_H \hbar^2 \tau_c}{r^6_{HH}} \quad (2)$$

where τ_c is the tumbling time of the protein; $R^F_{2,H}$ and $R^S_{2,H}$ are the fast and slow relaxing magnetization, respectively; γ_H is the gyromagnetic ratio of the proton; and r_{HH} is the distance between pairs of methyl protons.

In order to obtain an approximation of the differences in fast and slow relaxation rates (2η, we measured the time-dependence of the cross peak intensities in a correlated pair of single and double quantum (2Q) experiments (Tugarinov *et al.*, 2007). Using various delay time, *T,* values (3, 5, 8, 12, 17, 22, and 27 ms, recorded in an interleaved manner), the rates of η were obtained by fitting ratios of peak intensities measured in pairs of experiments (I_a and I_b, spin-forbidden and spin-allowed, respectively) with Eq. 3:

$$I_a/I_b = \frac{-0.5\eta\tanh\left(\sqrt{\eta^2+\delta^2}T\right)}{\sqrt{\eta^2+\delta^2}-\delta tanh\left(\sqrt{\eta^2+\delta^2}T\right)} \quad (3)$$

where T is the variable delay time, δ is a parameter that is related to the ^{1}H spin density around the methyl group, and I_a and I_b are the time dependencies of differences and sums, respectively, of magnetization derived from methyl ^{1}H single-quantum transitions, as described (Tugarinov *et al.*, 2007). Peak heights and spectral noise were measured in Sparky (Lee *et al.*, 2015). A python script was used to fit the peak height ratios to η values and to determine S^2_{axis} values in the apo- or Zn-bound states, as described previously (Tugarinov & Kay, 2004, Tugarinov *et al.*, 2007, Capdevila *et al.*, 2017a). τ_c was obtained from Monte Carlo simulations with tensor2 software (Dosset *et al.*, 2000), using T_1, T_2, and heteronuclear NOE (hNOE) recorded at 35 °C at 800 MHz, in 10% D_2O. To enable a direct comparison of each AdcR allosteric state while overcoming the difficulty of determining an isotropic τ_c from tensor2 for apo-AdcR (which harbors dynamically independent domains), the measured τ_c for each state was obtained by adjusting S^2_{axis} of alanine methyls to 0.85 since these methyl groups are generally motionally restricted in proteins (Igumenova *et al.*, 2006). For apo- and Zn^{II}_2 AdcRs, the τ_c obtained in this way is 18.9 ± 0.1 ns and 20.7 ± 0.1 ns respectively.

Relaxation dispersion measurements were acquired using a TROSY adaptation of ^{15}N and a ^{1}H-^{13}C HMQC-based Carr–Purcell–Meiboom–Gill (CPMG) pulse sequence for amides from the backbone (Tollinger *et al.*, 2001) and methyl groups from the sidechains (Korzhnev *et al.*, 2004), respectively. Experiments were performed at 35 °C at 600 and 800 MHz ^{1}H frequencies using constant time interval T=40 ms with CPMG field strengths (ν_{CPMG}) of 50, 100, 150, 200, 250, 300, 350, 400, 450, 500, 600, 700, 850, and 1,000 Hz. Data were fitted to the two-site fast exchange limit equation, as discussed previously (Capdevila *et al.*, 2017a). These experiments were performed on duplicate at the two field strengths.

DNA binding experiments and determination of allosteric coupling free energies (ΔG_c). For all DNA binding experiments a 28 bp double stranded DNA was obtained as previously described (Reyes-Caballero *et al.*, 2010) with the following sequence of the AdcO: 5'-TGATATAATTAACTGGTAAA CAAA ATGT[F]-3'. Apo AdcR binding experiments were conducted in solution conditions of 10 mM HEPES, pH 7.0, 0.23 M NaCl, 1 mM TCEP (chelexed), 10 nM DNA, 25.0 ºC with 2.0 mM EDTA (for apo-AdcR) or 20 μM $ZnCl_2$ (for Zn^{II}_2 AdcR) added to these reactions. Anisotropy experiments were performed on an ISS PC1 spectrofluorometer in steady-state mode with Glan-Thompson polarizers in the L-format. The excitation wavelength was set at 494 nm with a 1 mm slit and the total emission intensity collected through a 515 nm filter. For Zn(II)-bound-AdcR DNA-binding experiments, the data were fit with DynaFit (Kuzmic, 1996) using a non-dissociable dimer 1:1 dimer:DNA binding model (K_{dim}= 10^{12} M^{-1}). For Zn(II)-bound experiments, the initial anisotropy (r_0) was fixed to the measured value for the free DNA, with the anisotropy response of the saturated protein:DNA complex ($r_{complex}$) optimized during a nonlinear least squares fit using DynaFit (Kuzmic, 1996). Apo binding data were fit in the same manner, except $r_{complex}$ was fixed to reflect the anisotropy change ($r_{complex} - r_0$) observed for wild-type AdcR in the presence of zinc. The errors on $K_{apo,DNA}$ and $K_{Zn,DNA,}$ reflect the standard deviation of 3 independent titrations (Table S2). The coupling free energies were calculated using the following equation: $\Delta G_c = -RT\ln(K_{Zn,DNA}/K_{apo,DNA})$ (Giedroc & Arunkumar, 2007). Negative values of ΔG_c were observed since AdcR is a positive allosteric activator in the presence of Zn^{II} ($K_{apo,DNA} < K_{Zn,DNA,}$).

Acknowledgements

We gratefully acknowledge support of this work by the NIH (R35 GM118157 to D. P. G.). NMR instrumentation in the METACyt Biomolecular NMR Laboratory at Indiana University was generously supported by a grant from the Lilly Endowment. D.A.C. acknowledges support from the Pew Latin American Fellows Program in the Biomedical Sciences. We also thank Dr. Lixin Fan of the Small-Angle X-ray Scattering Core Facility, National Cancer Institute, Frederick, MD for acquiring the SAXS data.

References

Alekshun MN, Levy SB. 1999. Characterization of MarR superrepressor mutants. J Bacteriol. 181:3303-3306.

Alekshun MN, Levy SB. 2007. Molecular mechanisms of antibacterial multidrug resistance. Cell. 128:1037-1050.

Alekshun MN, Levy SB, Mealy TR, Seaton BA, Head JF. 2001. The crystal structure of MarR, a regulator of multiple antibiotic resistance, at 2.3 Å resolution. Nat Struct Biol. 8:710-714.

Anandapadamanaban M, Pilstål R, Andresen C, Trewhella J, Moche M, Wallner B, Sunnerhagen M. 2016. Mutation-induced population shift in the MexR conformational ensemble disengages DNA binding: A novel mechanism for MarR family derepression. Structure. 24:1311-1321.

Anderson KM, Esadze A, Manoharan M, Brüschweiler R, Gorenstein DG, Iwahara J. 2013. Direct observation of the ion-pair dynamics at a protein–DNA interface by NMR spectroscopy. J Am Chem Soc. 135:3613-3619.

Andresen C, Jalal S, Aili D, Wang Y, Islam S, Jarl A, Liedberg B, Wretlind B, Martensson LG, Sunnerhagen M. 2010. Critical biophysical properties in the *Pseudomonas aeruginosa* efflux gene regulator MexR are targeted by mutations conferring multidrug resistance. Protein Sci. 19:680-692.

Aranda J, Garrido ME, Fittipaldi N, Cortes P, Llagostera M, Gottschalk M, Barbe J. 2009. Protective capacities of cell surface-associated proteins of *Streptococcus suis* mutants deficient in divalent cation-uptake regulators. Microbiology. 155:1580-1587.

Arunkumar AI, Pennella MA, Kong X, Giedroc DP. 2007. Resonance assignments of the metal sensor CzrA in the apo-, Zn_2- and DNA-bound (42 kDa) states. Biomol NMR Assign. 1:99-101.

Birukou I, Seo SM, Schindler BD, Kaatz GW, Brennan RG. 2014. Structural mechanism of transcription regulation of the *Staphylococcus aureus* multidrug efflux operon *mepRA* by the MarR family repressor MepR. Nucleic Acids Res. 42:2774-2788.

Bordelon T, Wilkinson SP, Grove A, Newcomer ME. 2006. The crystal structure of the transcriptional regulator HucR from *Deinococcus radiodurans* reveals a repressor preconfigured for DNA binding. J Mol Biol. 360:168-177.

Campanello GC, Ma Z, Grossoehme NE, Guerra AJ, Ward BP, Dimarchi RD, Ye Y, Dann III CE, Giedroc DP. 2013. Allosteric inhibition of a zinc-sensing transcriptional repressor: Insights into the arsenic repressor (ArsR) family. J Mol Biol. 425:1143-1157.

Campbell E, Kaltenbach M, Correy GJ, Carr PD, Porebski BT, Livingstone EK, Afriat-Jurnou L, Buckle AM, Weik M, Hollfelder F, Tokuriki N, Jackson CJ. 2016. The role of protein dynamics in the evolution of new enzyme function. Nat Chem Biol. 12:944-950.

Capdevila DA, Braymer JJ, Edmonds KA, Wu H, Giedroc DP. 2017a. Entropy redistribution controls allostery in a metalloregulatory protein. Proc Natl Acad Sci U S A. 114:4424-4429.

Capdevila DA, Edmonds KA, Giedroc DP. 2017b. Metallochaperones and metalloregulation in bacteria. Essays Biochem. 61:177-200.

Caro JA, Harpole KW, Kasinath V, Lim J, Granja J, Valentine KG, Sharp KA, Wand AJ. 2017. Entropy in molecular recognition by proteins. Proc Natl Acad Sci U S A. 114:6563-6568.

Chakravorty DK, Parker TM, Guerra AJ, Sherrill CD, Giedroc DP, Merz KM, Jr. 2013. Energetics of zinc-mediated interactions in the allosteric pathways of metal sensor proteins. J Am Chem Soc. 135:30-33.

699 Chang YM, Jeng WY, Ko TP, Yeh YJ, Chen CK, Wang AH. 2010. Structural study of TcaR and
700 its complexes with multiple antibiotics from *Staphylococcus epidermidis*. Proc Natl Acad
701 Sci U S A. 107:8617-8622.
702 Chen PR, Bae T, Williams WA, Duguid EM, Rice PA, Schneewind O, He C. 2006. An
703 oxidation-sensing mechanism is used by the global regulator MgrA in *Staphylococcus*
704 *aureus*. Nat Chem Biol. 2:591-595.
705 Chin KH, Tu ZL, Li JN, Chou CC, Wang AH, Chou SH. 2006. The crystal structure of XC1739:
706 a putative multiple antibiotic-resistance repressor (MarR) from *Xanthomonas campestris*
707 at 1.8 Å resolution. Proteins. 65:239-242.
708 Clarke D, Sethi A, Li S, Kumar S, Chang RW, Chen J, Gerstein M. 2016. Identifying allosteric
709 hotspots with dynamics: Application to inter- and intra-species conservation. Structure.
710 24:826-837.
711 Cohen SP, Hachler H, Levy SB. 1993. Genetic and functional analysis of the multiple antibiotic
712 resistance (*mar*) locus in *Escherichia coli*. J Bacteriol. 175:1484-1492.
713 Delaglio F, Grzesiek S, Vuister GW, Zhu G, Pfeifer J, Bax A. 1995. NMRPipe: A
714 multidimensional spectral processing system based on UNIX pipes. J Biomol NMR.
715 6:277-293.
716 Deochand DK, Grove A. 2017. MarR family transcription factors: Dynamic variations on a
717 common scaffold. Crit Rev Biochem Mol Biol. 52:595-613.
718 Deochand DK, Perera IC, Crochet RB, Gilbert NC, Newcomer ME, Grove A. 2016. Histidine
719 switch controlling pH-dependent protein folding and DNA binding in a transcription
720 factor at the core of synthetic network devices. Mol BioSyst. 12:2417-2426.
721 Dolan KT, Duguid EM, He C. 2011. Crystal structures of SlyA protein, a master virulence
722 regulator of *Salmonella*, in free and DNA-bound states. J Biol Chem. 286:22178-22185.
723 Dosset P, Hus JC, Blackledge M, Marion D. 2000. Efficient analysis of macromolecular
724 rotational diffusion from heteronuclear relaxation data. J Biomol NMR. 16:23-28.
725 Duval V, McMurry LM, Foster K, Head JF, Levy SB. 2013. Mutational analysis of the multiple-
726 antibiotic resistance regulator marR reveals a ligand binding pocket at the interface
727 between the dimerization and DNA binding domains. J Bacteriol. 195:3341-3351.
728 Ellison DW, Miller VL. 2006. Regulation of virulence by members of the MarR/SlyA family.
729 Curr Opin Microbiol. 9:153-159.
730 Franke D, Svergun DI. 2009. DAMMIF, a program for rapid *ab-initio* shape determination in
731 small-angle scattering. J Appl Crystallogr. 42:342-346.
732 Frederick KK, Marlow MS, Valentine KG, Wand AJ. 2007. Conformational entropy in
733 molecular recognition by proteins. Nature. 448:325-329.
734 Fuangthong M, Helmann JD. 2002. The OhrR repressor senses organic hydroperoxides by
735 reversible formation of a cysteine-sulfenic acid derivative. Proc Natl Acad Sci U S A.
736 99:6690-6695.
737 Gao YR, Li DF, Fleming J, Zhou YF, Liu Y, Deng JY, Zhou L, Zhou J, Zhu GF, Zhang XE,
738 Wang DC, Bi LJ. 2017. Structural analysis of the regulatory mechanism of MarR protein
739 Rv2887 in *M. tuberculosis*. Sci Rep. 7:6471.
740 Giedroc DP, Arunkumar AI. 2007. Metal sensor proteins: Nature's metalloregulated allosteric
741 switches. Dalton Trans. 29:3107-3120.
742 Goddard TD, Kneller DG, Sparky 3. University of California, San Francisco.
743 Grove A. 2013. MarR family transcription factors. Curr Biol. 23:R142-R143.
744 Grove A. 2017. Regulation of metabolic pathways by MarR family transcription factors. Comput
745 Struct Biotechnol J. 15:366-371.

Guerra AJ, Dann CE, Giedroc DP. 2011. Crystal structure of the zinc-dependent MarR family transcriptional regulator AdcR in the Zn(II)-bound state. J Am Chem Soc. 133:19614-19617.

Guerra AJ, Giedroc DP. 2014. Backbone and sterospecific methyl side chain resonance assignments of the homodimeric zinc sensor AdcR (32 kDa) in the apo- and Zn(II)-bound states. Biomol NMR Assign. 8:11-14.

Gupta A, Grove A. 2014. Ligand-binding pocket bridges DNA-binding and dimerization domains of the urate-responsive MarR homologue MftR from *Burkholderia thailandensis*. Biochemistry. 53:4368-4380.

Hao Z, Lou H, Zhu R, Zhu J, Zhang D, Zhao BS, Zeng S, Chen X, Chan J, He C, Chen PR. 2013. The multiple antibiotic resistance regulator MarR is a copper sensor in *Escherichia coli*. Nat Chem Biol. 10:21-28.

Hong M, Fuangthong M, Helmann JD, Brennan RG. 2005. Structure of an OhrR-ohrA operator complex reveals the DNA binding mechanism of the MarR family. Mol Cell. 20:131-141.

Hyberts SG, Milbradt AG, Wagner AB, Arthanari H, Wagner G. 2012. Application of iterative soft thresholding for fast reconstruction of NMR data non-uniformly sampled with multidimensional Poisson Gap scheduling. J Biomol NMR. 52:315-327.

Igumenova TI, Frederick KK, Wand AJ. 2006. Characterization of the fast dynamics of protein amino acid side chains using NMR relaxation in solution. Chem Rev. 106:1672-1699.

Kalodimos CG, Biris N, Bonvin AM, Levandoski MM, Guennuegues M, Boelens R, Kaptein R. 2004. Structure and flexibility adaptation in nonspecific and specific protein-DNA complexes. Science. 305:386-389.

Kim Y, Joachimiak G, Bigelow L, Babnigg G, Joachimiak A. 2016. How aromatic compounds block DNA binding of HcaR catabolite regulator. J Biol Chem. 291:13243-13256.

Korzhnev DM, Kloiber K, Kanelis V, Tugarinov V, Kay LE. 2004. Probing slow dynamics in high molecular weight proteins by methyl-TROSY NMR spectroscopy: application to a 723-residue enzyme. J Am Chem Soc. 126:3964-3973.

Kuzmic P. 1996. Program DYNAFIT for the analysis of enzyme kinetic data: application to HIV proteinase. Anal Biochem. 237:260-273.

Lee W, Tonelli M, Markley JL. 2015. NMRFAM-SPARKY: enhanced software for biomolecular NMR spectroscopy. Bioinformatics. 31:1325-1327.

Liguori A, Malito E, Lo Surdo P, Fagnocchi L, Cantini F, Haag AF, Brier S, Pizza M, Delany I, Bottomley MJ. 2016. Molecular basis of ligand-dependent regulation of NadR, the transcriptional repressor of meningococcal virulence factor NadA. PLoS Pathog. 12:e1005557.

Liu G, Liu X, Xu H, Liu X, Zhou H, Huang Z, Gan J, Chen H, Lan L, Yang CG. 2017. Structural insights into the redox-sensing mechanism of MarR-type regulator AbfR. J Am Chem Soc. 139:1598-1608.

Llull D, Son O, Blanie S, Briffotaux J, Morello E, Rogniaux H, Danot O, Poquet I. 2011. *Lactococcus lactis* ZitR is a zinc-responsive repressor active in the presence of low, nontoxic zinc concentrations in vivo. J Bacteriol. 193:1919-1929.

Loo CY, Mitrakul K, Voss IB, Hughes CV, Ganeshkumar N. 2003. Involvement of the *adc* operon and manganese homeostasis in *Streptococcus gordonii* biofilm formation. J Bacteriol. 185:2887-2900.

Marijuan PC, Navarro J, del Moral R. 2010. On prokaryotic intelligence: strategies for sensing the environment. Biosystems. 99:94-103.

792 Motlagh HN, Wrabl JO, Li J, Hilser VJ. 2014. The ensemble nature of allostery. Nature.
793 508:331-339.
794 Otani H, Stogios PJ, Xu X, Nocek B, Li SN, Savchenko A, Eltis LD. 2016. The activity of
795 CouR, a MarR family transcriptional regulator, is modulated through a novel molecular
796 mechanism. Nucleic Acids Res. 44:595-607.
797 Pabis A, Risso VA, Sanchez-Ruiz JM, Kamerlin SC. 2018. Cooperativity and flexibility in
798 enzyme evolution. Curr Opin Struct Biol. 48:83-92.
799 Peng H, Zhang Y, Palmer LD, Kehl-Fie TE, Skaar EP, Trinidad JC, Giedroc DP. 2017.
800 Hydrogen sulfide (H2S) and reactive sulfur species (RSS) impact proteome *S*-
801 sulfhydration and global virulence regulation in *Staphylococcus aureus*. ACS Infect
802 Dis.3:744-755.
803 Perera IC, Grove A. 2010. Molecular mechanisms of ligand-mediated attenuation of DNA
804 binding by MarR family transcriptional regulators. J Mol Cell Biol. 2:243-254.
805 Perez-Rueda E, Collado-Vides J, Segovia L. 2004. Phylogenetic distribution of DNA-binding
806 transcription factors in bacteria and archaea. Comput Biol Chem. 28:341-350.
807 Quade N, Mendonca C, Herbst K, Heroven AK, Ritter C, Heinz DW, Dersch P. 2012. Structural
808 basis for intrinsic thermosensing by the master virulence regulator RovA of *Yersinia*. J
809 Biol Chem. 287:35796-35803.
810 Radhakrishnan A, Kumar N, Wright CC, Chou TH, Tringides ML, Bolla JR, Lei HT,
811 Rajashankar KR, Su CC, Purdy GE, Yu EW. 2014. Crystal structure of the transcriptional
812 regulator Rv0678 of *Mycobacterium tuberculosis*. J Biol Chem. 289:16526-16540.
813 Reyes-Caballero H, Guerra AJ, Jacobsen FE, Kazmierczak KM, Cowart D, Koppolu UM, Scott
814 RA, Winkler ME, Giedroc DP. 2010. The metalloregulatory zinc site in *Streptococcus*
815 *pneumoniae* AdcR, a zinc-activated MarR family repressor. J Mol Biol. 403:197-216.
816 Sanson M, Makthal N, Flores AR, Olsen RJ, Musser JM, Kumaraswami M. 2015. Adhesin
817 competence repressor (AdcR) from *Streptococcus pyogenes* controls adaptive responses
818 to zinc limitation and contributes to virulence. Nucleic Acids Res. 43:418-432.
819 Saridakis V, Shahinas D, Xu X, Christendat D. 2008. Structural insight on the mechanism of
820 regulation of the MarR family of proteins: high-resolution crystal structure of a
821 transcriptional repressor from *Methanobacterium thermoautotrophicum*. J Mol Biol.
822 377:655-667.
823 Schneidman-Duhovny D, Hammel M, Sali A. 2010. FoXS: a web server for rapid computation
824 and fitting of SAXS profiles. Nucleic Acids Res. 38:W540-544.
825 Seoane AS, Levy SB. 1995. Characterization of MarR, the repressor of the multiple antibiotic
826 resistance (*mar*) operon in *Escherichia coli*. J Bacteriol. 177:3414-3419.
827 Shen Y, Delaglio F, Cornilescu G, Bax A. 2009. TALOS+: a hybrid method for predicting
828 protein backbone torsion angles from NMR chemical shifts. J Biomol NMR. 44:213-223.
829 Sun F, Ding Y, Ji Q, Liang Z, Deng X, Wong CC, Yi C, Zhang L, Xie S, Alvarez S, Hicks LM,
830 Luo C, Jiang H, Lan L, He C. 2012. Protein cysteine phosphorylation of SarA/MgrA
831 family transcriptional regulators mediates bacterial virulence and antibiotic resistance.
832 Proc Natl Acad Sci U S A. 109:15461-15466.
833 Takano H, Mise K, Maruyama T, Hagiwara K, Ueda K. 2016. Role of the semi-conserved
834 histidine residue in the light-sensing domain of LitR, a MerR-type photosensory
835 transcriptional regulator. Microbiology. 162:1500-1509.
836 Tamber S, Cheung AL. 2009. SarZ promotes the expression of virulence factors and represses
837 biofilm formation by modulating SarA and *agr* in *Staphylococcus aureus*. Infect Immun.
838 77:419-428.

Tollinger M, Skrynnikov NR, Mulder FAA, Forman-Kay JD, Kay LE. 2001. Slow dynamics in folded and unfolded states of an SH3 domain. J Am Chem Soc. 123:11341-11352.

Tugarinov V, Kay LE. 2003. Ile, Leu, and Val methyl assignments of the 723-Residue malate synthase G using a new labeling strategy and novel NMR methods. J Am Chem Soc 125:13868-13878.

Tugarinov V, Kay LE. 2004. $^{1}H,^{13}C$-$^{1}H,^{1}H$ dipolar cross-correlated spin relaxation in methyl groups. J Biomol NMR. 29:369-376.

Tugarinov V, Sprangers R, Kay LE. 2007. Probing side-chain dynamics in the proteasome by relaxation violated coherence transfer NMR spectroscopy. J Am Chem Soc. 129:1743-1750.

Tzeng SR, Kalodimos CG. 2009. Dynamic activation of an allosteric regulatory protein. Nature. 462:368-372.

Tzeng SR, Kalodimos CG. 2012. Protein activity regulation by conformational entropy. Nature. 488:236-240.

Tzeng SR, Kalodimos CG. 2013. Allosteric inhibition through suppression of transient conformational states. Nat Chem Biol. 9:462-465.

Ulrich LE, Koonin EV, Zhulin IB. 2005. One-component systems dominate signal transduction in prokaryotes. Trends Microbiol. 13:52-56.

Weatherspoon-Griffin N, Wing HJ. 2016. Characterization of SlyA in *Shigella flexneri* identifies a novel role in virulence. Infect Immun. 84:1073-1082.

West AL, Evans SE, Gonzalez JM, Carter LG, Tsuruta H, Pozharski E, Michel SL. 2012. Ni(II) coordination to mixed sites modulates DNA binding of HpNikR via a long-range effect. Proc Natl Acad Sci U S A. 109:5633-5638.

Wilke MS, Heller M, Creagh AL, Haynes CA, McIntosh LP, Poole K, Strynadka NCJ. 2008. The crystal structure of MexR from *Pseudomonas aeruginosa* in complex with its antirepressor ArmR. Proc Natl Acad Sci U S A. 105:14832-14837.

Wishart DS, Sykes BD. 1994. Chemical shifts as a tool for structure determination. Methods Enzymol. 239:363-392.

Yoon H, McDermott JE, Porwollik S, McClelland M, Heffron F. 2009. Coordinated regulation of virulence during systemic infection of *Salmonella enterica* serovar Typhimurium. PLoS Pathog. 5:e1000306.

Zhu R, Hao Z, Lou H, Song Y, Zhao J, Chen Y, Zhu J, Chen PR. 2017a. Structural characterization of the DNA-binding mechanism underlying the copper(II)-sensing MarR transcriptional regulator. J Biol Inorg Chem. 22:685-693.

Zhu R, Hao Z, Lou H, Song Y, Zhao J, Zhu J, Chen PR. 2017b. Structural and mechanistic study of the cysteine oxidation-mediated induction of the *Escherichia coli* MarR regulator. Tetrahedron. 73:3714-3719.

Zhu R, Song Y, Liu H, Yang Y, Wang S, Yi C, Chen PR. 2017c. Allosteric histidine switch for regulation of intracellular zinc(II) fluctuation. Proc Natl Acad Sci U S A. 114:13661-13666.

Figure Legends

Figure 1. (a) Ribbon representation of dimeric Zn(II)-bound AdcR, with one protomer shaded white and the other shaded *light blue* (PDB-ID: 3tgn) (Guerra *et al.*, 2011). The two Zn(II) ions in each protomer are represented by spheres, and coordinating ligands are shown in stick representation. The DNA binding helices are shaded *red*. (b) Simplified free energy diagram showing of the active (*green*) and inactive (*blue*) states the relative population of two distinct conformations: compatible with DNA binding (*red* rectangle, α4-α4' distance between DNA binding helices, ≈30 Å) and incompatible with DNA binding (larger α4-α4' distances). (c) The α4-α4' distance distribution plotted against the DNA-binding inter-helical α4-α4' orientation distribution for all the reported MarR crystal structures (see Table S1 for details) in the allosterically "active" DNA-binding conformation (*green*), an "inactive" conformation (*blue*) and in the DNA-bound (*red*) conformation. The inferred conformational space occupied by the DNA-bound conformation in all MarR regulators (Table S1) is shaded in *red* oval. Ribbon representation of the molecules in each conformation are shown in the inset, as well as a scheme of how the distances and angles were measured. (d) Histogram plot of the α4-α4' distance (see panel c) extracted from 136 different crystal structures of MarR repressors in the DNA-binding-"inactive", DNA-binding "active" and DNA-bound conformations.

Figure 2. (a) Small angle X-ray scattering (SAXS) curve of AdcR in apo- and Zn_2-states, with a curve calculated from the previously published AdcR-Zn_2 structure (Fig. 1A, PDB-ID: 3tgn) (Guerra *et al.*, 2011). Best-fit DAMMIF *ab initio* model(Franke & Svergun, 2009) for apo- (b) (*blue*) and Zn^{II}_2-states (c) (*green*), aligned with the ribbon representation of the Zn^{II}_2 structure

(Fig. 1A, PDB-ID: 3tgn). The corresponding Guinier, Kratky and pairwise distribution histogram plots are shown in Fig. S2, along with the fitting parameters.

Figure 3. Chemical shift perturbation maps for Zn^{II} binding to AdcR for the backbone (a) and the sterospecifically assigned methyl groups (b) at pH 5.5, 50 mM NaCl, 35 ºC. CSPs are painted on the ribbon representation of the structure of Zn^{II}_2 AdcR. The shaded bar in each case represents one standard deviation from the mean perturbation. Site 1 and site 2 ligands in the primary structure in panel (a) are denoted by the *yellow* and *green* circles, respectively; the asterisks at residue positions 21 and 38-40 indicate no assignment in the apo-state (see Materials and Methods). (c) Distribution of α1-α2 loops lengths in the reported structures in all MarR family of proteins (see Table S1 for an accounting of these structures). A postulated schematic representation of allosteric inhibition and activation are shown (*inset*), with shorter α1-α2 loops driving allosteric inhibition of the DNA binding upon ligand binding, and longer loops associated with allosteric activation (like that for AdcR/ZitR) upon ligand binding.

Figure 4. Dynamical characterization of the apo- (a) (c) (e) and Zn^{II}_2 (b) (d) (f) AdcR conformational states. Backbone ^{1}H-^{15}N amide R_2/R_1 for apo- (a) and Zn^{II}_2 AdcR (b) painted onto the 3tgn structure (Guerra *et al.*, 2011). Heteronuclear NOE analysis of apo- (c) and Zn^{II}_2 (d) AdcR with the values of the ^{15}N-{^{1}H}-NOE (hNOE) painted onto the 3tgn structure. Values of R_{ex} determined from HSQC ^{15}N-^{1}H CPMG relaxation dispersion experiments at a field of 600 MHz for the apo- (e) and Zn^{II}_2 (f) AdcRs (see Fig. S6 for complete data). Similar results were obtained at 800 MHz (Fig. S6). Zn^{II} ions are shown as black spheres and residues excluded due to overlapped are shown in gray and yellow. The width of the ribbon reflects the value represented in the color bar.

Figure 5. Effect of Zn^{II} binding to AdcR on the site-specific stereospecifically assigned methyl group axial order parameter, S^2_{axis} (a) and R_{ex} (b) plotted as ΔS^2_{axis} ($S^2_{axis}{}^{Zn} - S^2_{axis}{}^{apo}$) and ΔR_{ex} ($R_{ex}{}^{Zn} - R_{ex}{}^{apo}$) values, respectively, mapped onto the structure of Zn^{II}_2 AdcR (3tgn). A $\Delta S^2_{axis} < 0$ indicates that the methyl group becomes *more* dynamic in the Zn^{II}_2-bound state, while $\Delta R_{ex} < 0$ indicates quenching of motion on the μs-ms timescale in the in the Zn^{II}_2-bound state. See Fig. S5 for a graphical representation of all S^2_{axis} and R_{ex} values in each conformation from which these differences were determined, and Fig. S6 for summary of all dynamical parameters measured here. Residues harboring methyl groups that show major dynamical perturbations on Zn^{II} binding are highlighted, with selected residues subjected to cavity mutagenesis (Fig. 6; Table S2).

Figure 6. Graphical summary of the functional properties of AdcR cavity and hydrogen bonding mutants. (a) Zoom of the DNA binding domain (DBD) of one of the two Zn^{II}_2-bound AdcR protomers highlighting the residues targeted for mutagenesis (cavity mutants, *red stick*; hydrogen-bonding pathway mutants, *green stick*; zinc ligand E24, *yellow stick*), with the helical elements (α1-α5) indicated. (b) Cα positions of the residues targeted for cavity mutagenesis in the DNA binding domain (DBD) (*red spheres*) and in the dimerization domain (DIM) (*blue spheres*); other residues targeted for substitution in the hydrogen-bonding pathway (N38, Q40; *green spheres*) and zinc ligand E24 (*yellow spheres*) highlighted on the structure of the Zn^{II}_2 ZitR-DNA operator complex (Zhu *et al.*, 2017c); Zn^{II} ions (*black spheres*). (c) Coupling free energy analysis for all AdcR mutants highlighted using the same color scheme as in panels (a), (b). DBD, DNA-binding domain; DIM, dimerization domain; H-bond, hydrogen binding mutants. Lower horizontal line, K_{DNA} for wild-type apo-AdcR; upper horizontal line, K_{DNA} for

wild-type Zn^{II}_2 AdcR, for reference. The trend in ΔS2axis and ΔRex is qualitatively indicated (see Table S2). These residues are conserved to various degrees in AdcR-like repressors (Fig. S12).

Figure 7. Entropically driven model for how conformational dynamics can be harnessed to evolve allosteric activation (*upper right*) vs. allosteric inhibition (*lower right*) in the same molecular scaffold. This model suggests that dynamic properties of the active states have been conserved to give rise to a more favorable conformational entropy. In the metalloregulatory MarRs (AdcR, ZitR), the inactive state shows perturbed dynamics over a range of timescales; apo-AdcR therefore exhibits low affinity for DNA. Metal ion (*yellow circle*) coordination quenches both local and global modes in the dimerization domain and linkers, while inducing conformational disorder in the DNA-binding domain that enhances DNA binding affinity, thus stabilizing a conformation that has high affinity for DNA and giving rise to a favorable conformational entropy. For prototypical MarRs, where the ligand (*yellow star*) is an allosteric inhibitor, ligand binding narrows the conformational ensemble to a DNA-binding "inactive" conformation decreasing the enthalpic contribution to DNA binding, while perturbing fast time scale dynamics that give rise to an unfavorable conformational entropy for DNA-binding.

975 **FIGURES**

976 **Figure 1**

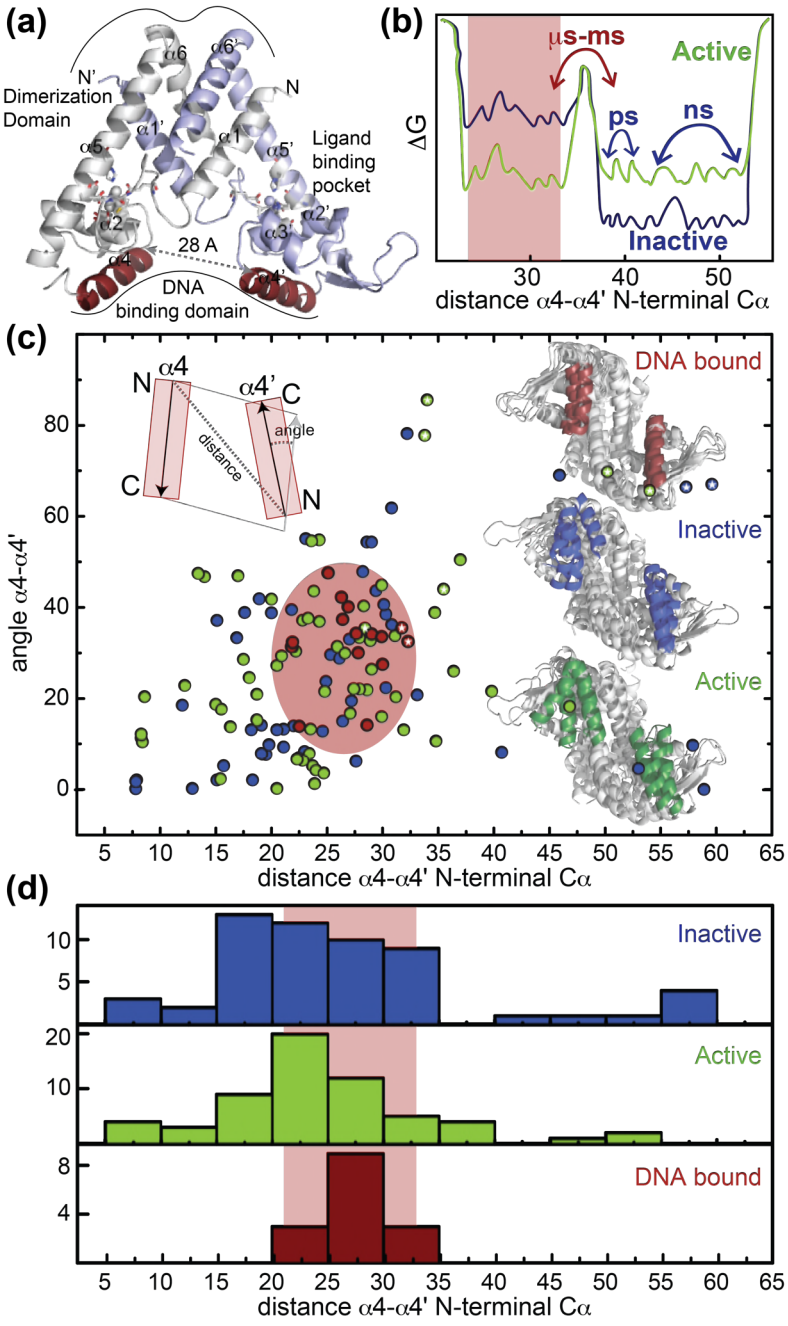

977

978 **Figure 2**

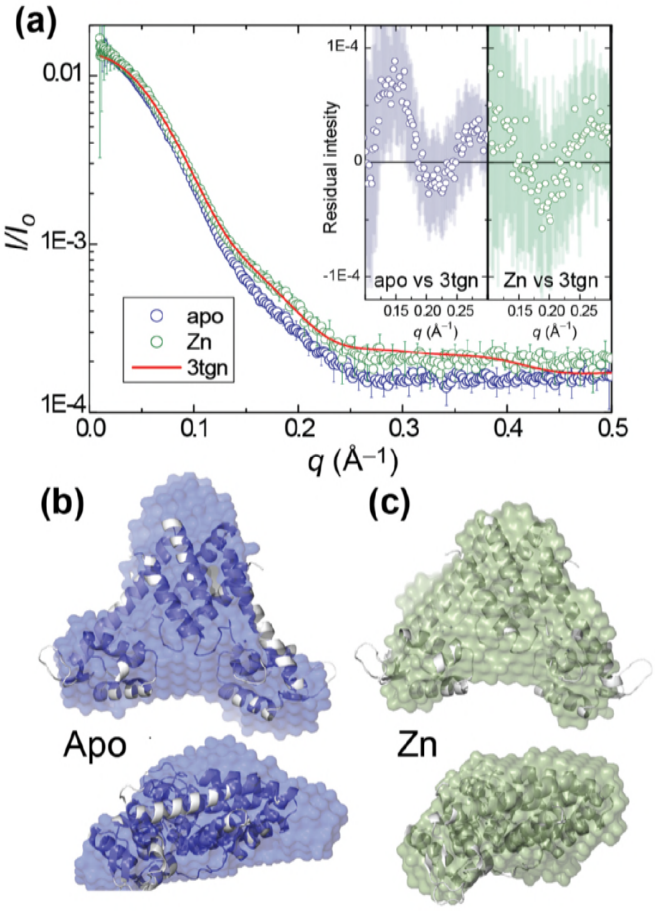

979 **Figure 3**

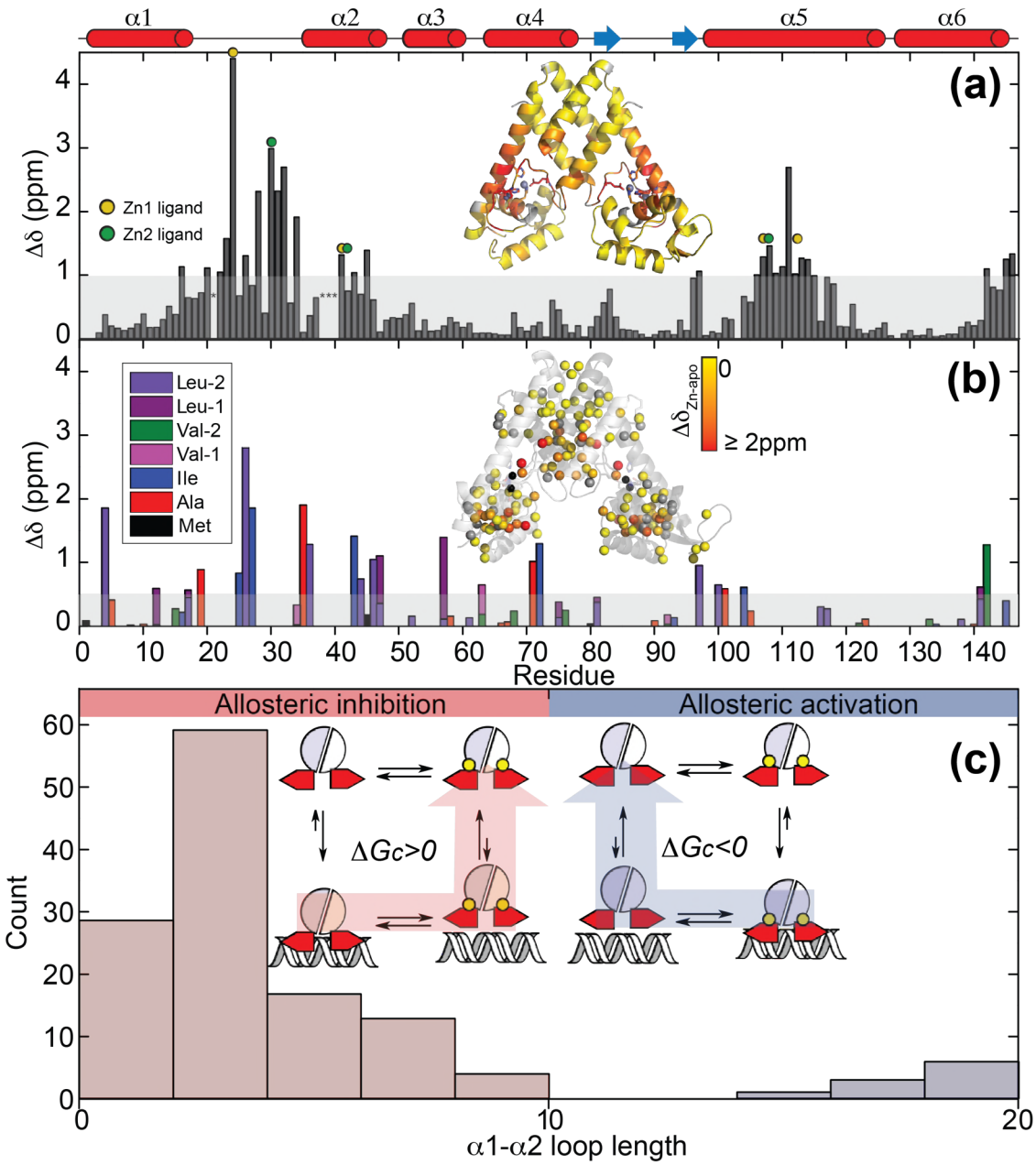

980

981 **Figure 4**

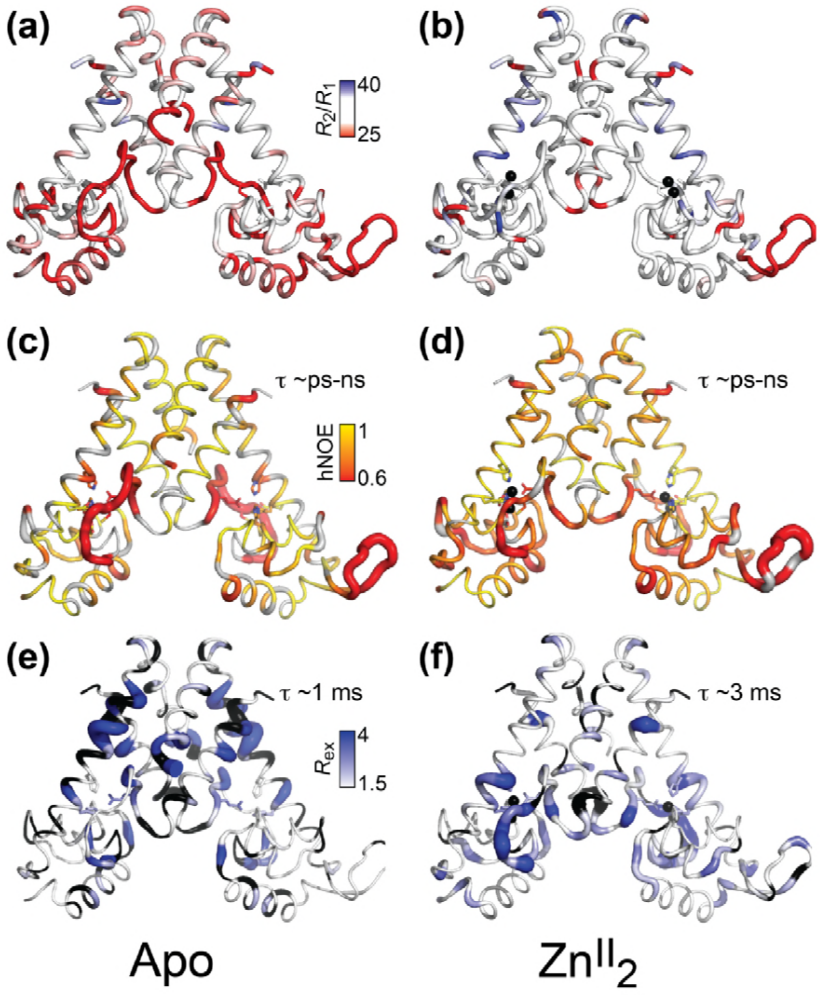

982

983

984

985 **Figure 5**

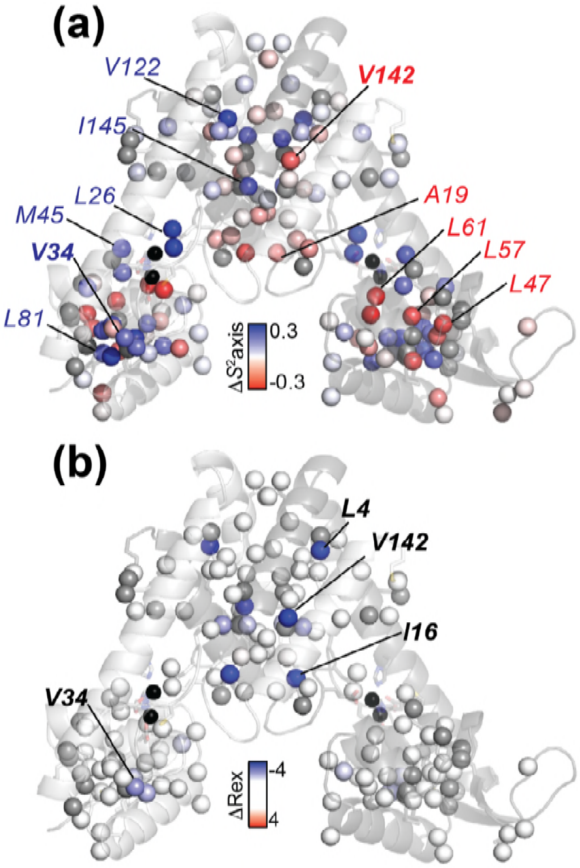

986

987 .

988

989 **Figure 6**

990

991

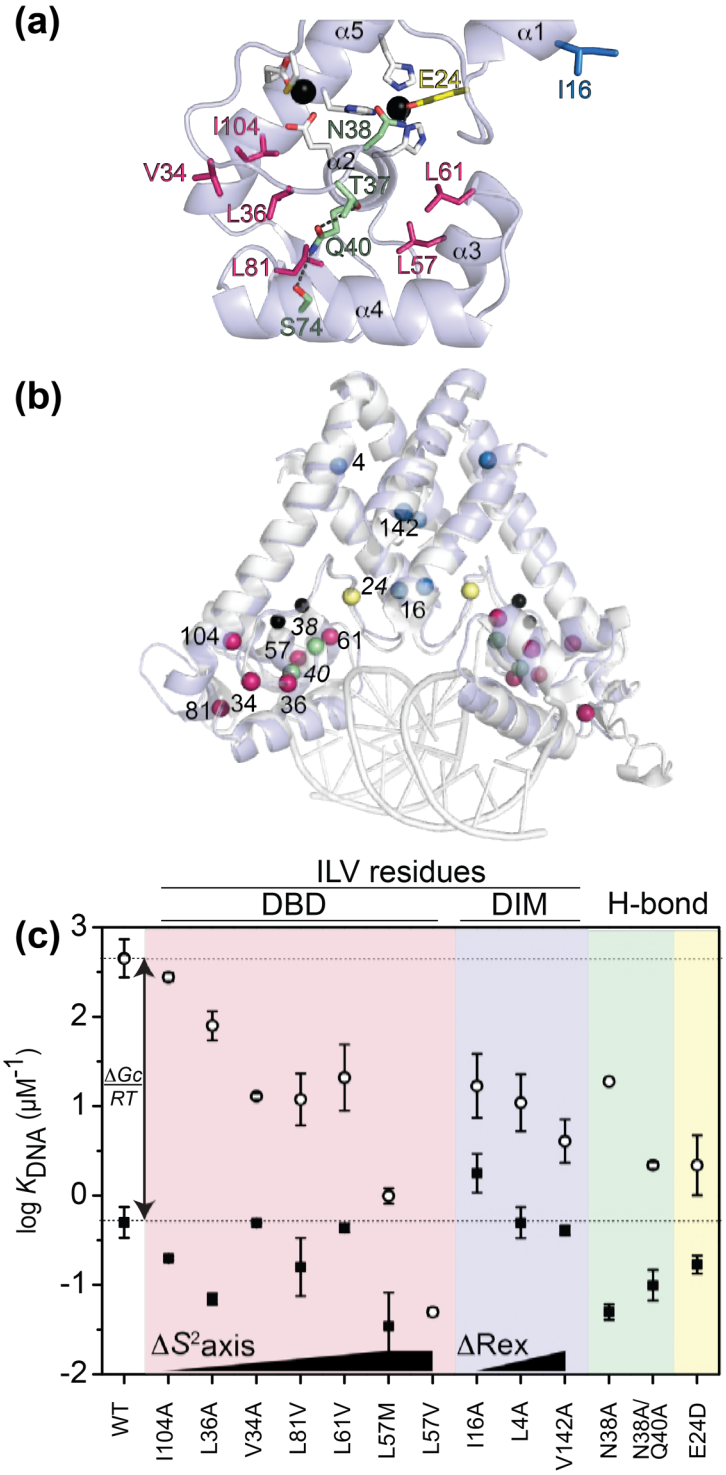

992 **Figure 7**

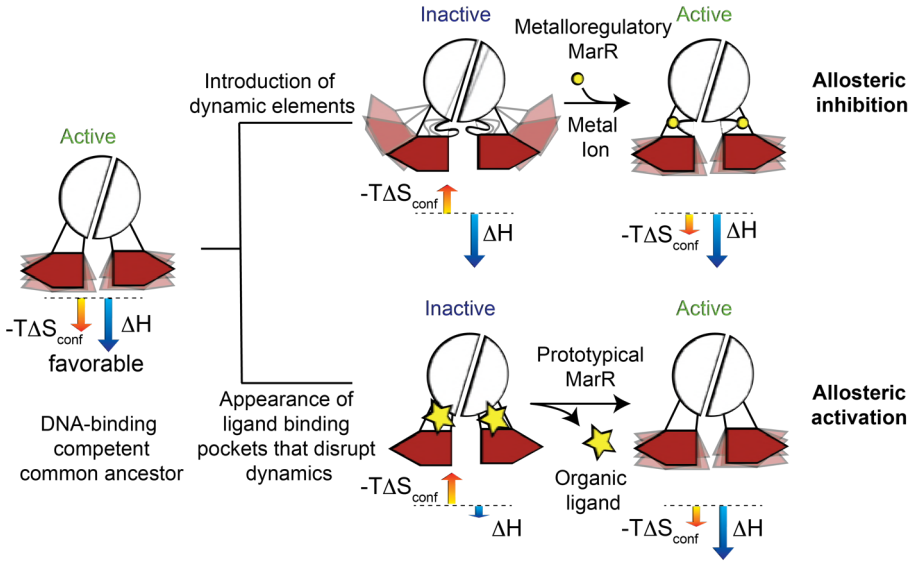

993

994

Supplementary Data

Tuning site-specific dynamics to drive allosteric activation in a pneumococcal zinc uptake regulator

Daiana A. Capdevila,[†] Fidel Huerta,[†,‡] Katherine A. Edmonds,[†] My T. Le,[†] Hongwei Wu,[†] and David P. Giedroc*[,†,§]

This file contains **Supplementary Tables S1-S3** and **Supplementary Figures S1-S12**.

Table S1. Interprotomer distances between the Cα of the N-terminal residue in the α4 and α4' helices

	DNA-bound state		Inhibited state[a]		Active state[b]	
MarR	Distance (Å)	PDB ID	Distance (Å)	PDB ID	Distance (Å)	PDB ID
ZitR (AdcR)	32.3/31.7	5yi2/5yi3	59.6/57.3	5yh0/5yh1	35.5/54.0/ 50.2 (22.2/ 34/ 33.8)	5yhx/5yhy/ 5yhz (3tgn/5jls/ 5jlu)
Ec MarR	29	5hr3	12.9 / 12	1jgs/4jba	8.3 / 8.4	3vod/3voe
OhrR	27.6	1z9c	(32.2)	(2pfb)	23.9 (28.9)	1z91 (2pex)
SlyA	27.8	3q5f	29.4	3deu	15.5 (23.8, 20)	3qpt (1lj9, 4mnu)
AbsC	26.3	3zpl	30.8	3zmd	-	-
RovA	21.8 / 21.9	4aij/ 4aik	-	-	20.9	4aih
MosR	25.1	4fx4	15.1	4fx0	-	-
MepR	26.4 / 26.9	4lll/ 4lln	18.9/16.9/ 30.8/57.9	3eco/4l9n/ 4l9t/4l9v	27.9 / 46.8	4l9j/4ld5
AbfR	29.9 / 30	5hlh/5hlg	40.7	5hli	37	4hbl
Rv2887	22.5	5hso	7.9 / 15.1	5hsn/5hsl	8.3	5hsm
HcaR	28.6	5bmz	19.1 / 19.8 / 19.5 / 19.2	4rgx /4rgu / 4rgs/ 4rgr	18.7	3k0l
ST1710	10.1[c]	3gji	23	3gf2	22.8	2eb7
TcaR	19.1[d]	4kdp	22.3/24.7	4eju/3kp7	26.4/22.5/ 21.1/ 22/ 27.6/18.3/ 21.1/ 18.2	3kp2/ 3kp3/ 3kp4/ 3kp5/ 3kp7/ 4ejt/ 4ejv/ 4ejw

[a]Proposed or measured DNA binding constant below 10^6 M^{-1}. [b] Proposed or measured DNA binding constant above 10^7 M^{-1}. [c] Not inserted in the major groove of the DNA. [d]This structure was co-crystallized with ssDNA.

Table S2. DNA binding parameters for wild-type AdcR and substitution mutants[a]

AdcR	$K_{apo,DNA}$ (x10^6 M^{-1})	Zn^{II}		Dynamic changes (Zn^{II})		Fractional ASA[b]
		$K_{Zn,\ DNA}$ (x10^6 M^{-1})	ΔG_c (kcal mol^{-1})	ΔS^2_{axis}	ΔRex	
wild-type	0.5 ± 0.2	450 ± 220	–4.0 ± 0.6			
I104A	0.20 ± 0.01	280 ± 30	–4.3 ± 0.4	-0.08 ± 0.01	0.3	0.04
L36A	0.07 ± 0.01	80 ± 30	–4.1 ± 0.4	0.15 ± 0.02	3.2	0.05
V34A	0.5[c] ± 0.01	13 ± 1	–2.2 ± 0.3	0.15 ± 0.02	3.5	0.46
L81V	0.16 ± 0.12	12 ± 8	–2.4 ± 0.6	0.20 ± 0.02	0	0.00
L61V	0.44 ± 0.05	21 ± 18	–2.3 ± 0.1	-0.247 ± 0.001	-0.7	0.01
L57M	0.035 ± 0.030	1 ± 0.2	–2.0± 0.7	-0.30 ± 0.02	0.7	0.00
L57V	<0.05[d]	<0.05[d]	N/A	-0.30 ± 0.02	0.7	0.00
I16A	1.8 ± 0.9	17 ± 14	–1.8 ± 0.4	-0.07 ± 0.01	3.5	0.11
L4A	0.5 ± 0.2	11 ± 8	–1.8 ± 0.3	0.02 ± 0.02	4	0.01
V142A	0.41 ± 0.05	4.1 ± 2.3	–1.4 ± 0.2	-0.095 ± 0.005	7	0.31
N38A	0.05 ± 0.01	19 ± 10	–3.5 ± 0.7	–[e]	–	–
N38A/Q40A	0.10 ± 0.04	2.2 ± 0.4	–1.9 ± 0.2	–	–	–
E24D	0.17 ± 0.04	2.2 ± 1.7	–1.6 ± 0.3	–	–	–

[a]Conditions: 10 mM Hepes, pH 7.0, 0.23 M NaCl, 1 mM TCEP (chelexed), 10 nM DNA, 25.0 ºC with 2.0 mM EDTA (for apo-AdcR) or 20 μM $ZnCl_2$ (for Zn^{II}_2 AdcR) added to these reactions. See Fig. 6C, main text, for a graphical representation of these data. [b]Accessible surface area (ASA) calculated from the Zn^{II}_2-bound AdcR (Guerra *et al.*, 2011). [c]Upper limit on measureable $K_{apo,DNA}$ under these solution conditions. [d]Weaker than upper limit. [e]Not measurable using the NMR experiments employed here.

Table S3. Zinc binding affinities of wild-type AdcR and selected AdcR mutants characterized here.

AdcR	Zn^{II} binding to site 2 in the homodimer	
	$K_{Zn,3}$ ($x10^9$ M^{-1})	$K_{Zn,4}$ ($x10^9$ M^{-1})
wild-type	≥1	0.0205 ±0.0013
V34A	0.0022±0.0017	(9.4±8.2) 10^{-5}
L81V	≥1	0.025±0.0027
L61V	≥1	0.0181±0.0022
L57M	≥1	0.0169±0.001
L57V	≥1	0.119±0.018
I16A	≥1	0.00479±0.0005
V142A	0.00085±0.00018	$<10^{-5}$

[a]Conditions: 10 mM Hepes, pH 7.2, 0.4 M NaCl, 1 mM TCEP (chelexed), 15 μM Mf2, 25.0 ºC titrated with $ZnCl_2$ solutions. Experiments were conducted 3 times for each AdcR variant. Errors of the binding constant parameters were estimated from global fits.

[b] $K_{Zn,1}$ and $K_{Zn,2}$ were fixed to a value of 1 $x10^{12}$ M^{-1}. [c] $K_{Zn,MF2}$ = (4.9 ± 0.6) $x10^6$ M^{-1} under these solution conditions.

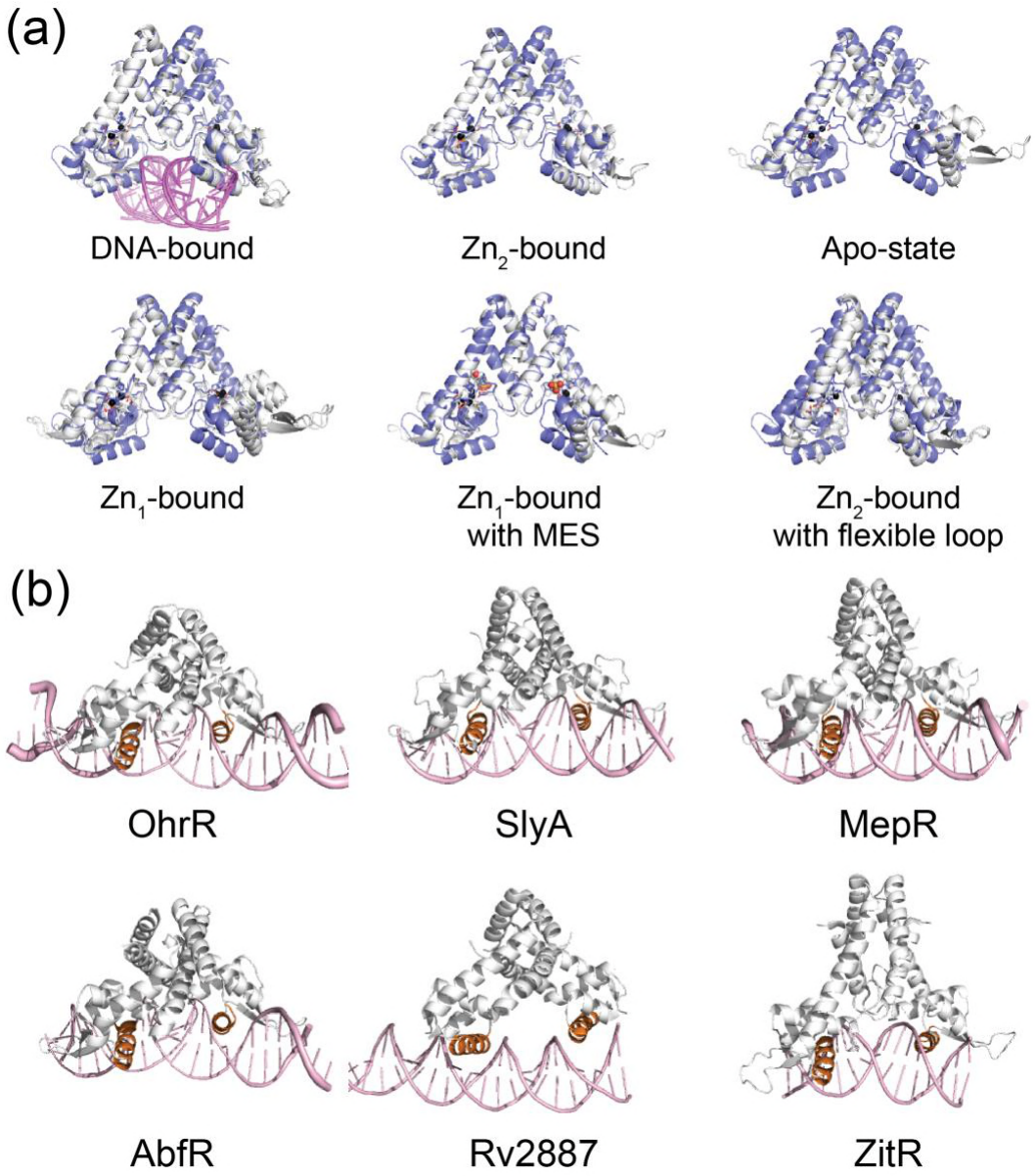

Figure S1. (a) Structural comparison (global superposition) between AdcR (3tgn, shaded *slate* in all panels, (Guerra *et al.*, 2011)) and *L. lactis* ZitR (Zhu *et al.*, 2017) in the different allosteric states (DNA-bound PDB codes, 5yi2, 5yi3; Zn^{II}_2-bound, 5hyx; Apo-state, 5yi1; Zn_1-bound PDB ID 5yhy, 5yl0; Zn^{II}_2-bound alternative state with a MES molecule in Zn site 1, 5yhz; Zn_2-bound from Group A *Streptococcus pyogenes* AdcR (Sanson *et al.*, 2015) with flexible loop, 5jls, 5lju). (b) Structural comparisons of various MarR family repressors in the DNA-bound states. (*B. subtilis* OhrR, PDB code, 1z9c; *S. enterica* SlyA, 3q5f; *S. aureus* MepR, 4lln; *S. epidermis* AbfR, 5hlg; *M. tuberculosis* Rv2887, 5hso; *L. Lactis* ZitR, 5yi2.

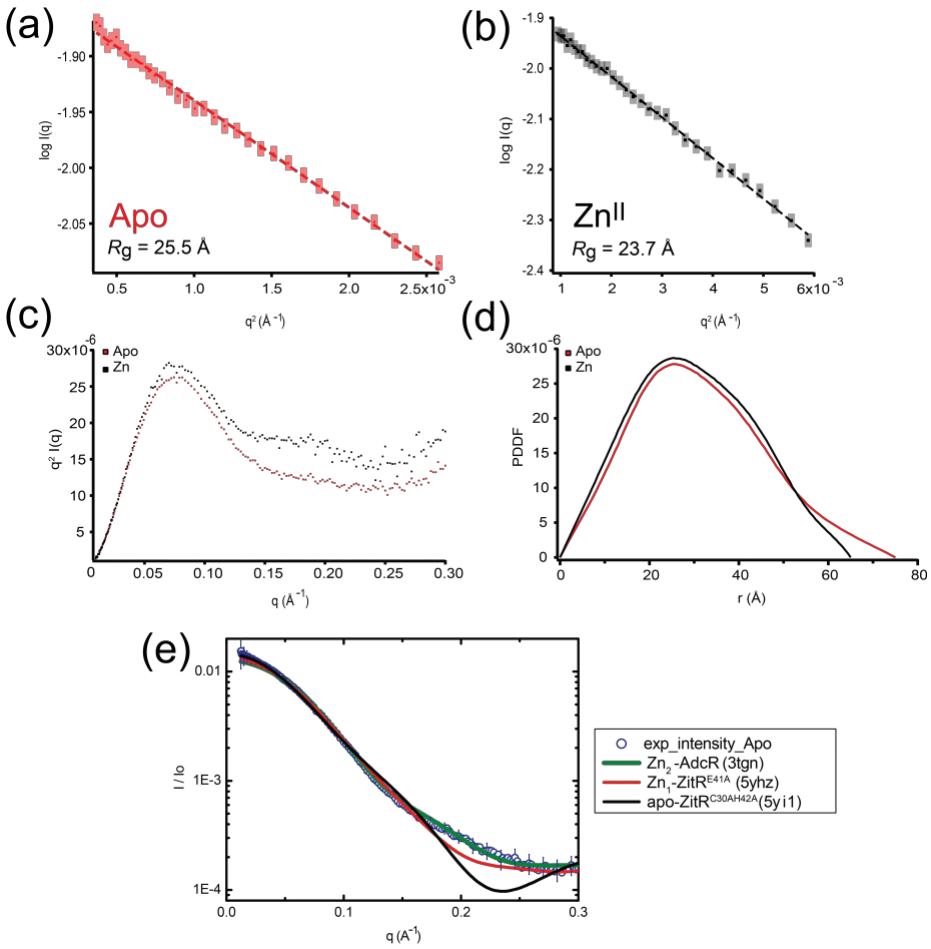

Figure S2. Small angle X-ray scattering (SAXS) analysis of AdcR in apo and Zn-binding states. (a) The Guinier region with linear fit of the scattering curve of the AdcR apo state (red) and Zn-binding state (black). Radius of gyration (Rg) of each state is presented at the low left corner. Note that scattering intensity is in arbitrary unit. (b) Dimensolionless Kratky plot of the AdcR apo (red) and Zn-binding (red) state. (c) Pair distance distribution function (PDDF) of the AdcR apo (red) and Zn-binding (black) state. The end-to-end distance (D_{max}) of apo state is 65 Å and D_{max} of the Zn-binding state is 75 Å. (d) Scattering profiles of AdcR apo (red) and Zn-binding states and (e) calculated scattering profiles of crystal structures of apo ZitR^{C30AH42A} (5yi1) and Zn-binding ZitR^{E41A} (5yhz) (Zhu *et al.*, 2017) compared to the experimental and fitted curves obtained for apo-AdcR (see **Fig. 2**, main text).

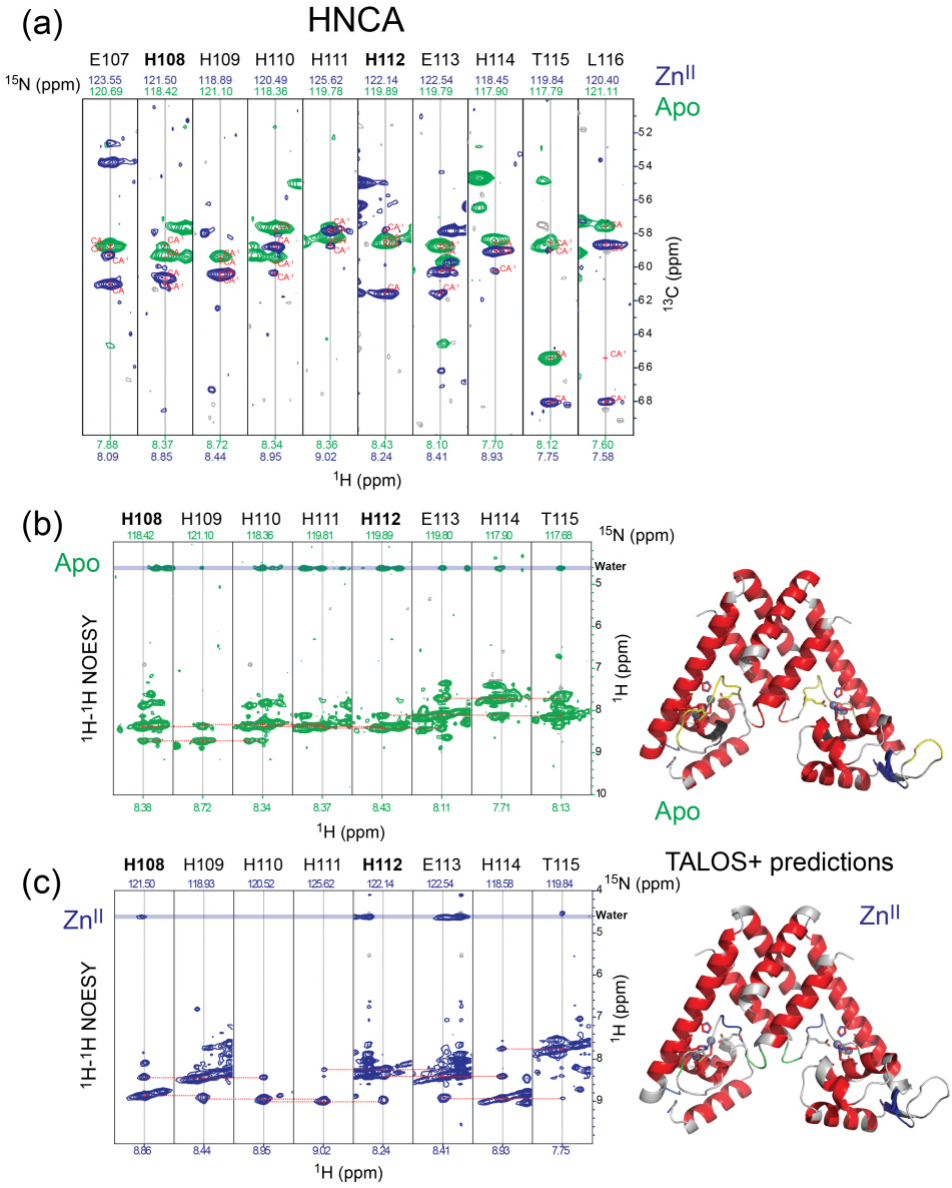

Figure S3. (a) Sequential residue-specific connectivities that link the chemical shifts of the ^{13}Cα resonances in the α5 helix (E107-L116; H108, H112 Zn^{II} ligands in bold) from an HNCA experiment. (b), (c) ^{1}H,^{15}N NOESY-HSQC strips obtained from the same region of the α5 helix in the apo- (b) and Zn^{II}_2 (c) states. *Right*, TALOS+ predictions in the apo- (top) and Zn^{II}_2 (bottom) states. Despite fully α-helical predictions, the apo-state is characterized by weaker i, *i+2* NH-NH correlations, and stronger NOEs (as solvent exchange crosspeaks) to water, relative to the Zn^{II} state. This is consistent with a more highly dynamic α5 helix in the apo-state.

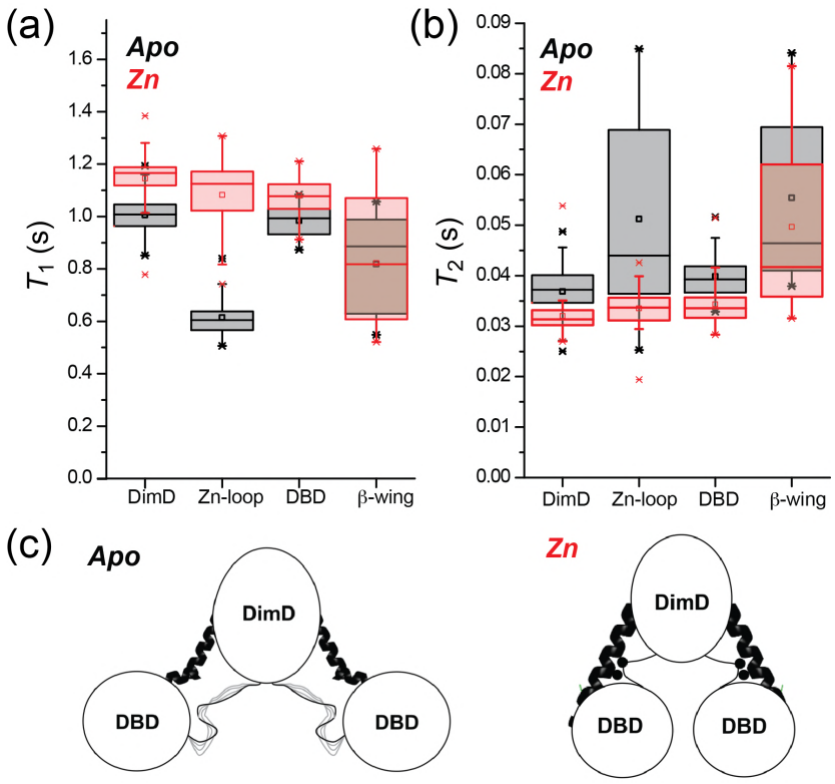

Figure S4. Average backbone amide ^{1}H-^{15}N relaxation parameters T_1 ($1/R_1$, a) and T_2 ($1/R_2$, b) for the apo- (*black* boxes) and Zn^{II}_2- (*red* boxes) states of the AdcR homodimer in different regions of the molecule: DimD, dimerization domain (residues 5-20, 101-144); Zn-loop (α1-α2 loop, residues 21-37); DBD, DNA binding domain (residues 38-101, excluding the β-wing; β-wing (residues 81-101). (c) Cartoon representations of the data shown in panels (a) and (b) in which the two linkers that connect the two domains (middle of the α5-helix, *dark coil*; α1-α2 loop, *light pencil*) are more dynamic in the apo-state. Note that residues analogous to the α1-α2 loop in AdcR are not observed in the crystal structure of the apo-state of *L. lactis* ZitR (Zhu *et al.*, 2017) (see Fig. S1A), consistent with these findings in solution in apo-AdcR.

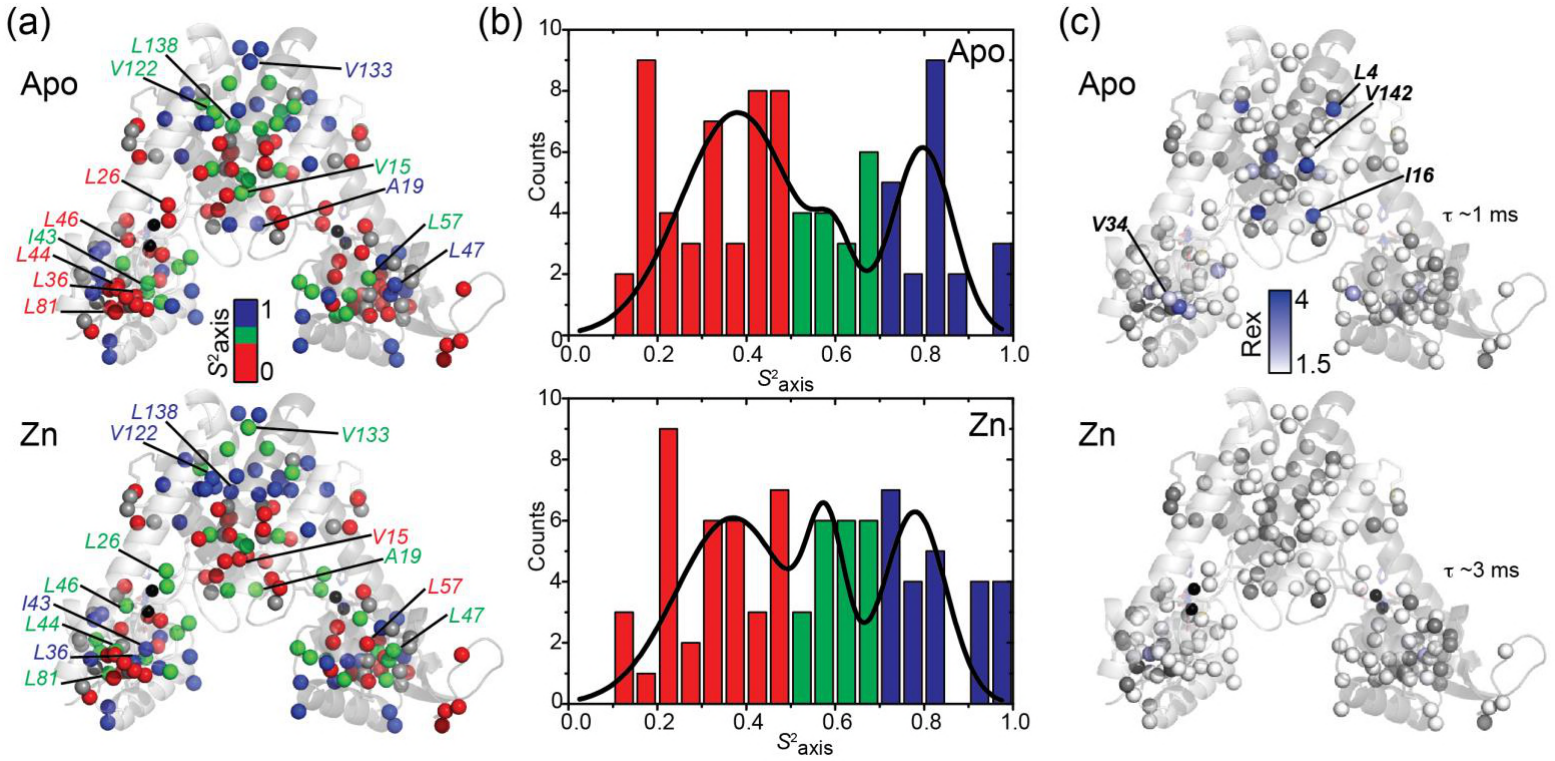

Figure S5. Absolute values of methyl group order parameters, S^2_{axis} (a) and R_{ex} (c) on the methyl-bearing residues. (b) Histogram plot of S^2_{axis} from fitting the apo (*top*) and Zn^{II}_2 (*bottom*) states in panel (a) calculated according to (Marlow *et al.*, 2010).

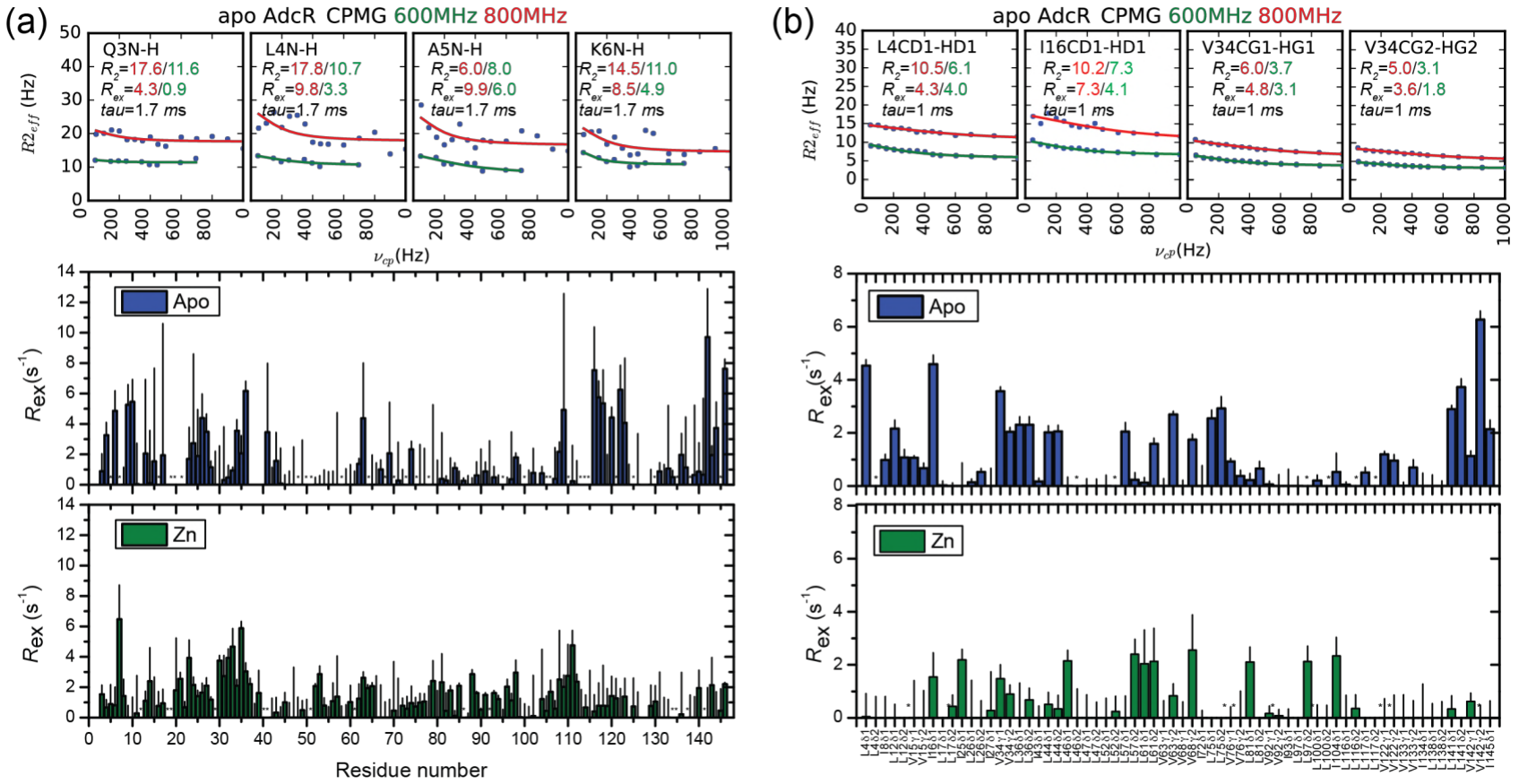

Figure S6. Representative raw relaxation dispersion curves obtained for the indicated backbone (NH) (a) or methyl group (b) used to obtain R_{ex} at 600 MHz and 800 MHz. R_{ex} for both allosteric states at 600 MHz are shown in each panel. All the residues excluded due to overlap are shown with an asterisk (Backbone Apo: 5, 7, 16, 18, 19, 22, 48, 50, 51, 58, 64, 68, 70, 73, 75, 78, 95, 100, 105, 106, 110, 113, 114, 115, 121, 125, 130, 135, 138, 145; Backbone Zn-bound: 12, 18, 19, 29, 40, 41, 51, 61, 86, 92, 134, 135, 137, 141; Sidechain Apo: L4-δ2, L46-δ2, L52-δ2, L97-δ2, L100-δ2, L116-δ2, L117-δ2; Sidechain Zn-bound: L12-δ2, L17-δ1,L57-δ1, L75-δ1, L75-δ2, L81-δ2, L97-δ1, L117-δ1, L117-δ2, L141-δ2).

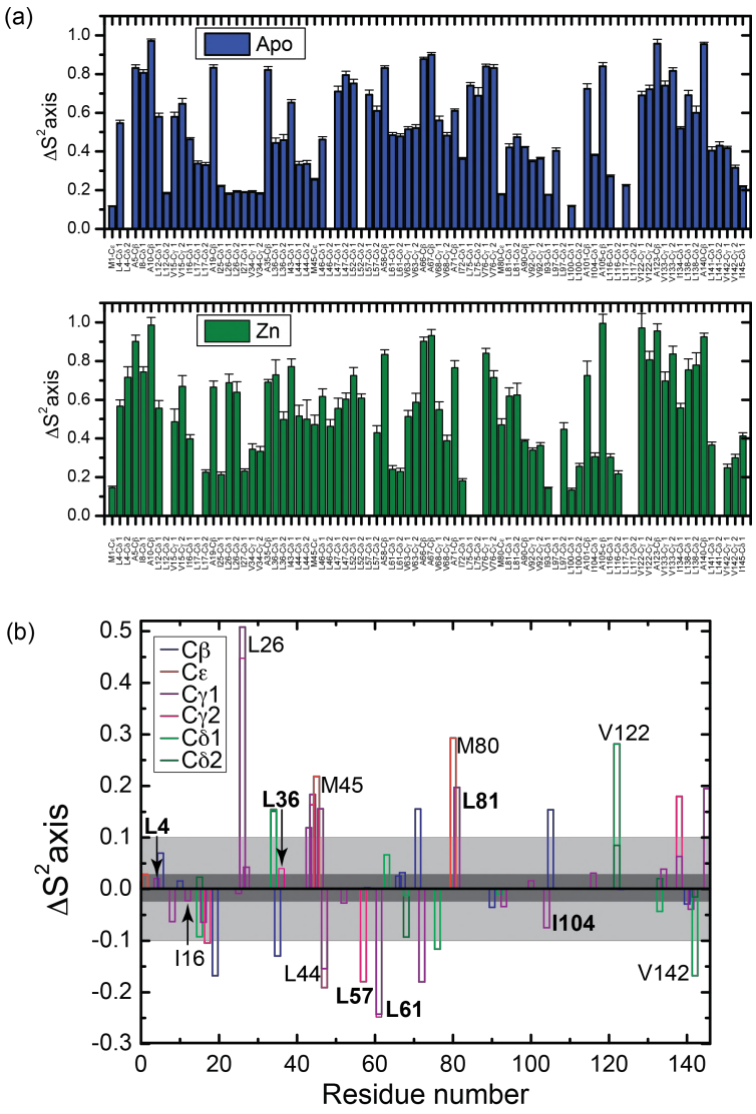

Figure S7. (a) Stereospecific methyl group axial order parameters, S^2_{axis}, for apo- and Zn^{II}_2-AdcR as measured at 600 MHz (similar results were obtained at 800 MHz; data not shown). (b) Difference in axial order parameter ($\Delta S^2_{axis} = S^2_{axis}{}^{Zn} - S^2_{axis}{}^{apo}$) between apo- and Zn^{II}_2-states, with the specific type of methyl group color-coded as indicated: Cβ, Ala; Cε, Met; Cγ1, Cγ2, Val; Cδ1, Cδ2, Leu.

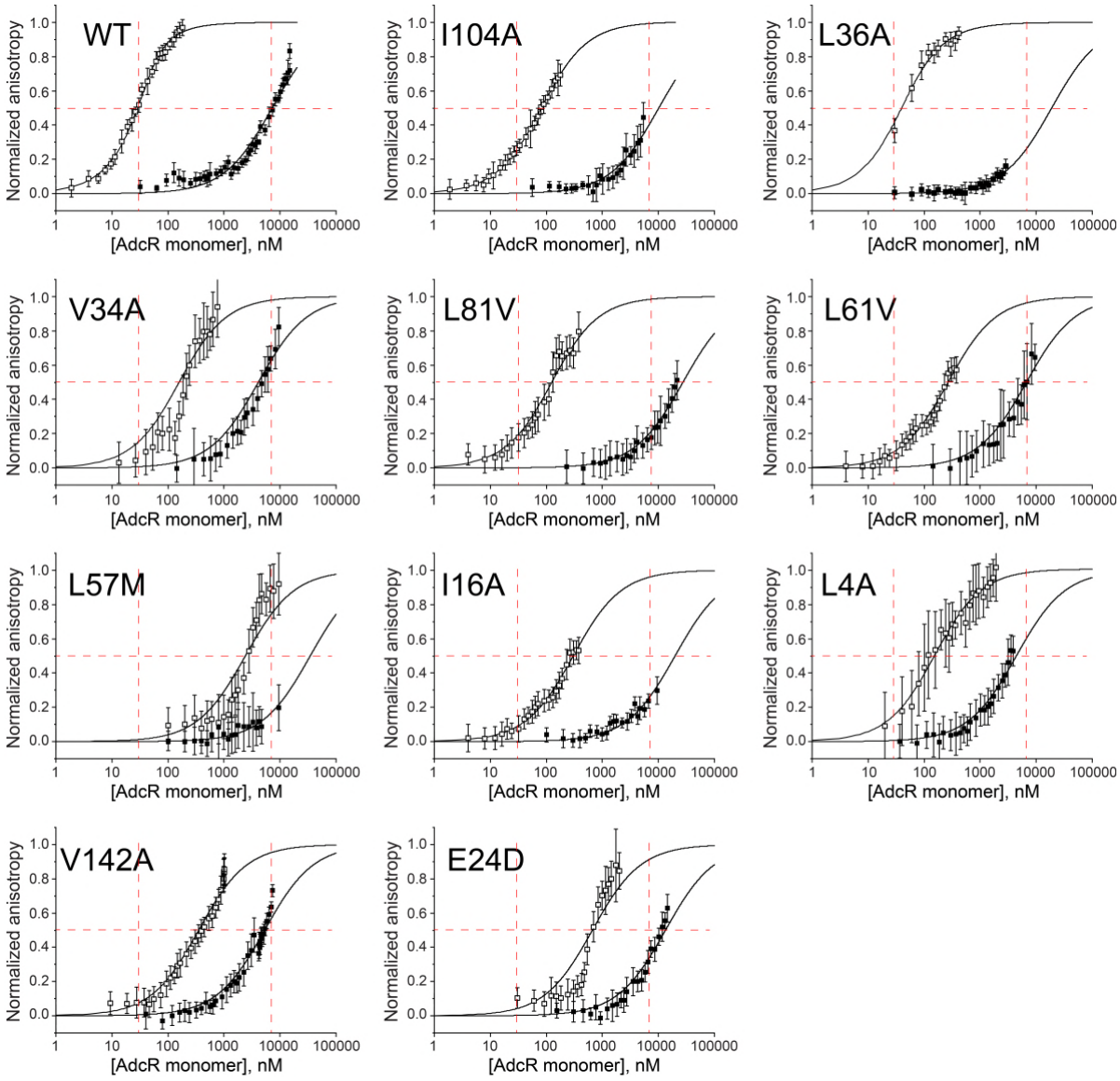

Figure S8. Representative DNA operator binding isotherms obtained for selected for wild-type (WT) AdcR and selected AdcR mutants in the apo- and Zn^{II}_2-states. The *continuous* lines through each set of data correspond to nonlinear least squares fit to a 1:1 non-dissociable AdcR dimer binding model, with parameters compiled in Table S2, and ΔG_c shown graphically in Fig. 6c (**main text**). The *red vertical and horizontal lines* represent the AdcR monomer concentrations that correspond to 50% DNA-saturation points for the wild-type AdcR under the same solution conditions, presented as a guide only. Conditions: 10 mM Hepes, pH 7.0, 0.23 M NaCl, 1 mM TCEP (chelexed), 10 or 20 nM nM DNA, 25.0 ºC with 1.0 mM EDTA (for apo-AdcR) or 20 μM $ZnCl_2$ (for Zn^{II}_2 AdcR) added to these reactions. Experiments were conducted 3 times for each AdcR variant.

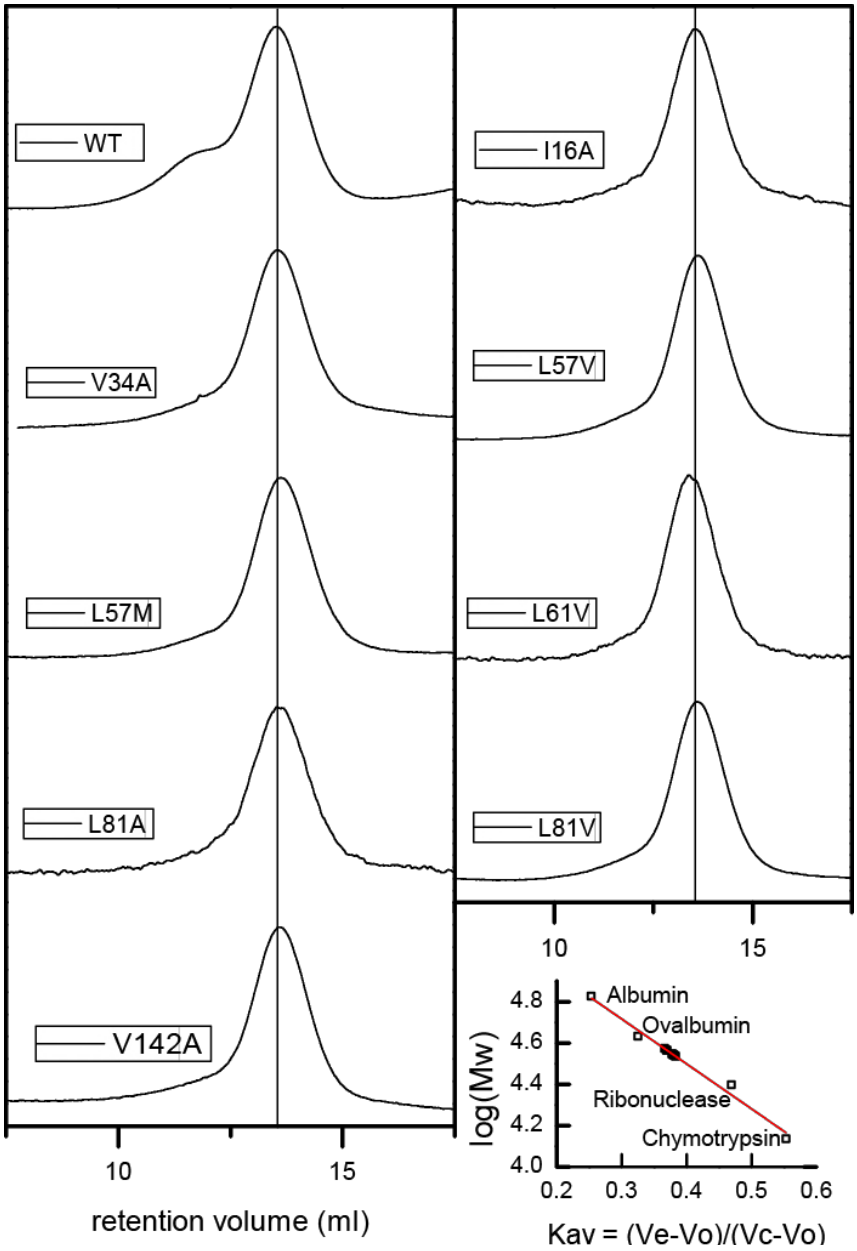

Figure S9. Gel filtration chromatograms for AdcR variants in the apo-state. *Lower right,* calibration curve with standards (empty squares) and AdcR variants (*filled* squares).

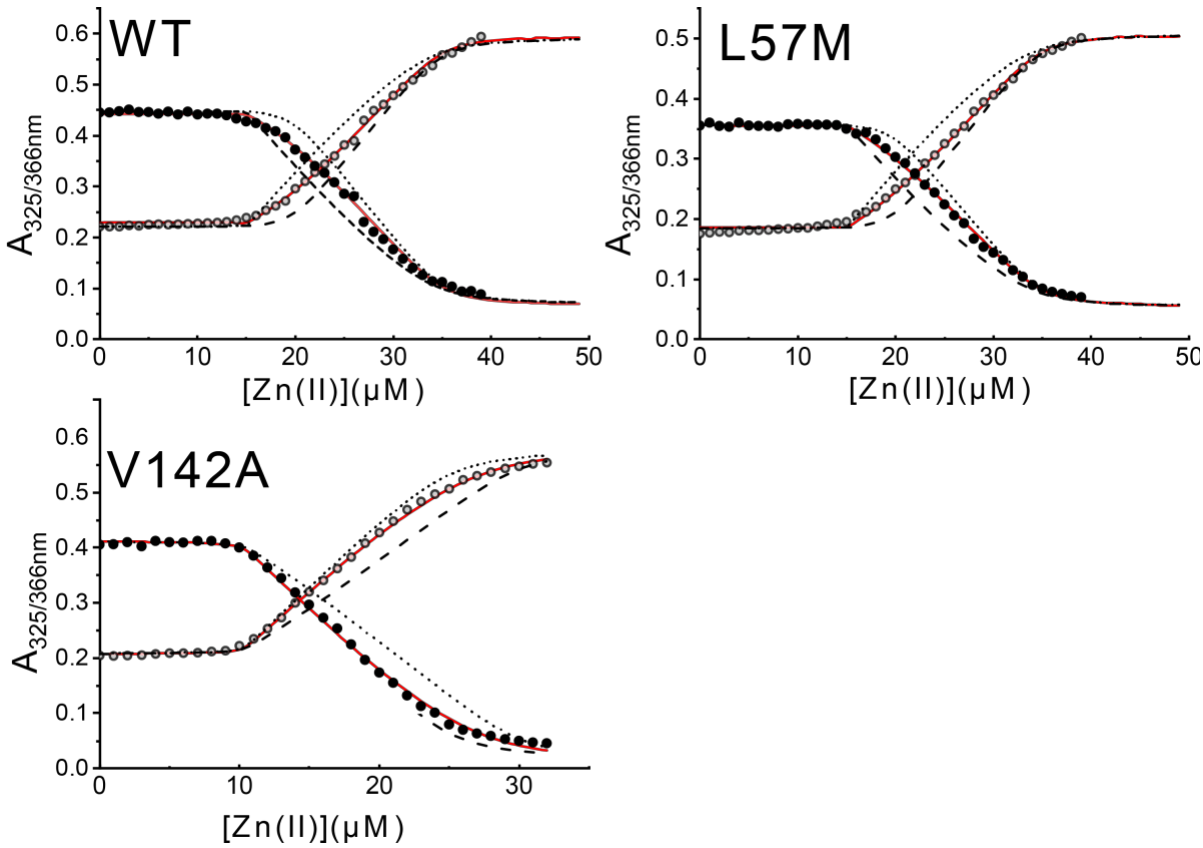

Figure S10. Representative Zn^{II}-binding isotherms obtained from a titration of apo (metal-free) wild-type AdcR or a mutant AdcR and mag-fura-2 (mf2) with $ZnSO_4$. Zn^{II} binding parameters for these and other AdcRs are compiled in Table S3. Experiments were conducted 3 times for each AdcR variant.

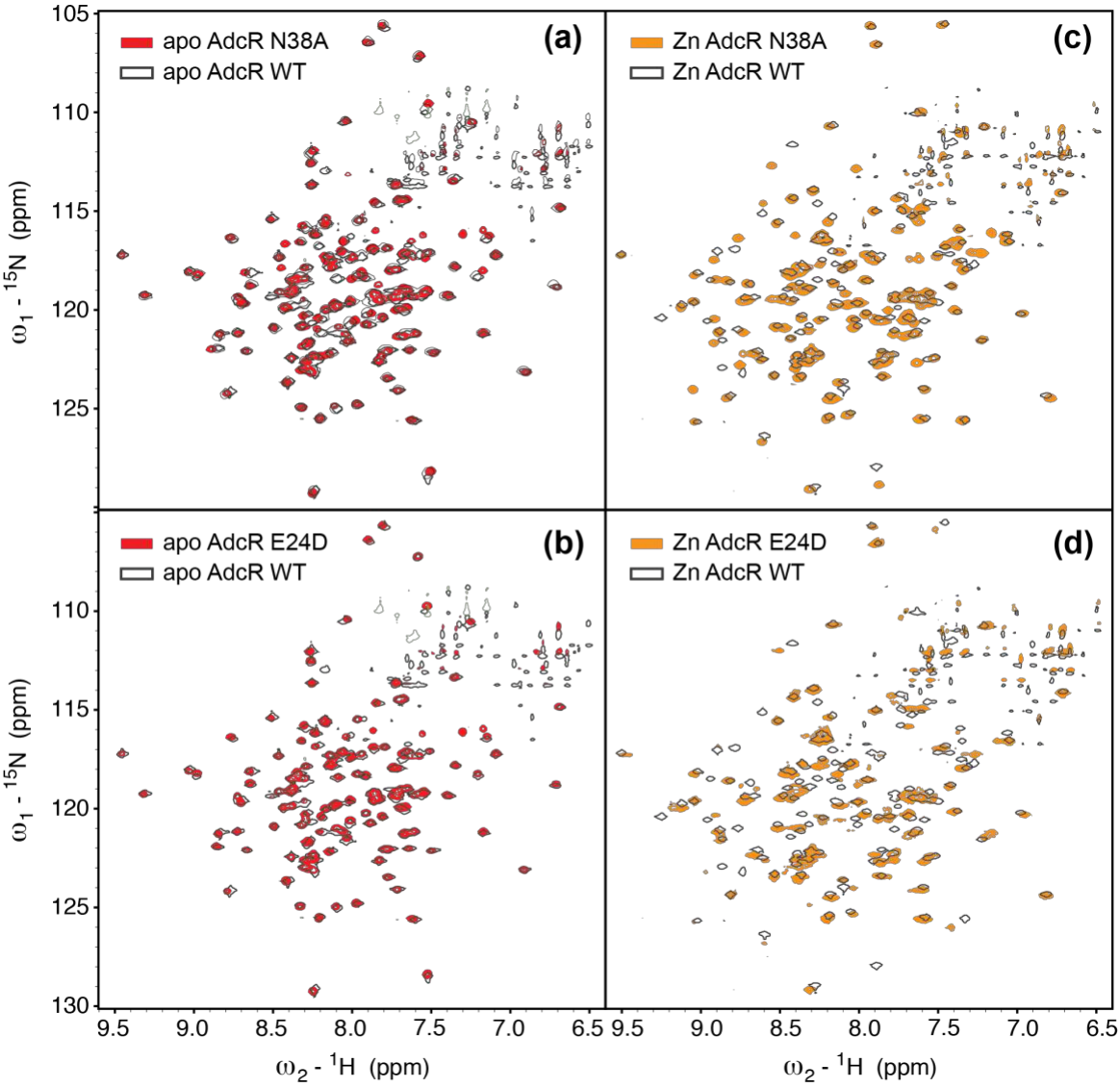

Figure S11. 2D $^{1}H,^{15}N$ TROSY spectra of apo- (*left*) and Zn^{II}_{2} (*right*) states of N38A and E24D AdcRs, compared to the wild-type AdcR (*black* contour; since contour line shown) acquired under the same solution conditions (50 mM NaCl, pH 6.0, 35 ºC).

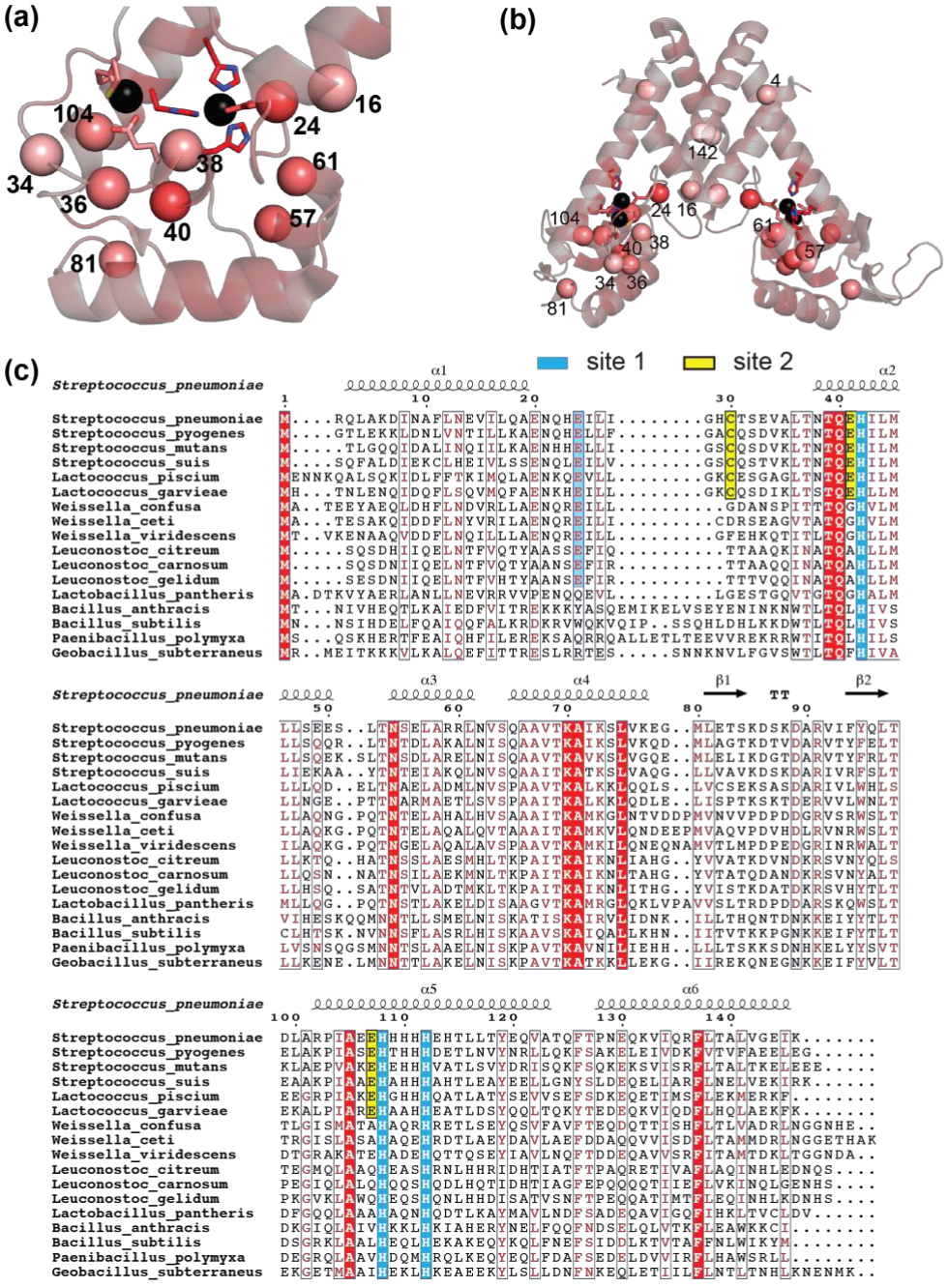

Figure S12. Amino acid sequence conservation of *S. pneumoniae* AdcR and candidate closely related MarR family repressors. Sequence conservation highlighting those residues targeted for mutagenesis in this work with a Cα sphere on the Zn^{II}_2 AdcR structure (Guerra *et al.*, 2011) in the DNA binding domain (a) and the entire molecule (b). The ribbon structure shows the degree of conservation by ramping the color from *white* to *bright red*, with those residues of high conservation shaded *bright red*, using Protskin (Ritter *et al.*, 2004). For reference, Zn^{II} ligands are invariant (100% conserved). (b) Multiple sequence analysis of the 17 AdcR-like repressors used to create the sequence conservation map.

References

Guerra AJ, Dann CE, Giedroc DP. 2011. Crystal structure of the zinc-dependent MarR family transcriptional regulator AdcR in the Zn(II)-bound state. J Am Chem Soc. 133:19614-19617.

Marlow MS, Dogan J, Frederick KK, Valentine KG, Wand AJ. 2010. The role of conformational entropy in molecular recognition by calmodulin. Nat Chem Biol. 6:352-358.

Ritter B, Denisov AY, Philie J, Deprez C, Tung EC, Gehring K, McPherson PS. 2004. Two WXXF-based motifs in NECAPs define the specificity of accessory protein binding to AP-1 and AP-2. EMBO J. 23:3701-3710.

Sanson M, Makthal N, Flores AR, Olsen RJ, Musser JM, Kumaraswami M. 2015. Adhesin competence repressor (AdcR) from *Streptococcus pyogenes* controls adaptive responses to zinc limitation and contributes to virulence. Nucleic Acids Res. 43:418-432.

Zhu R, Song Y, Liu H, Yang Y, Wang S, Yi C, Chen PR. 2017. Allosteric histidine switch for regulation of intracellular zinc(II) fluctuation. Proc Natl Acad Sci U S A. 114:13661-13666.

147